Evidence for centennial-scale Mid-Holocene episodes of hypolimnetic anoxia in a high-altitude lake system from central Tian Shan (Kyrgyzstan)

Philippe Sorrel, Kevin Jacq, Antonin van Exem, Gilles Escarguel, Benjamin Dietre, Maxime Debret, Suzanne Mcgowan, Ducept Jules, Gauthier Emilie, Hedi Oberhänsli

Evidence for centennial-scale Mid-Holocene episodes of hypolimnetic anoxia in a high-altitude lake system from Central Tian Shan (Kyrgyzstan)

Philippe Sorrel[a], Kévin Jacq[b], Antonin Van Exem[b], Gilles Escarguel[c], Benjamin Dietre[d], Maxime Debret[b], Suzanne McGowan[e], Jules Ducept[a], Emilie Gauthier[f] and Hedi Oberhänsli[g]

[a] Univ Lyon, Univ Lyon 1, ENSL, CNRS, LGL-TPE, F-69622, Villeurbanne, France

[b] Normandie Univ, UNIROUEN, UNICAEN, CNRS, M2C, 76000 Rouen, France

[c] Univ Lyon, Université Claude Bernard Lyon 1, CNRS, ENTPE, UMR 5023 LEHNA, F-69622, Villeurbanne, France

[d] Institut für Botanik, Universität Innsbruck, Sternwartestrasse 15, 6020 Innsbruck, Austria

[e] School of Geography, University of Nottingham, University Park, Nottingham, UK

[f] UMR 6249, Laboratoire Chrono-environnement, 16 route de Gray, 25030 Besançon cedex, France

[g] Museum für Naturkunde, Leibnitz-Institute Berlin (Mineralogy), Invalidenstrasse 43, 10115 Berlin, Germany

*Corresponding author: P. Sorrel; philippe.sorrel@univ-lyon1.fr

Keywords

Hyperspectral imaging, Paleolimnology, Paleoclimate, Lake stratification, Hypolimnetic anoxia, Chemocline, Central Asia, Lake Son Kol, Holocene

Abstract

Few sedimentary archives of lake meromixis are available in palaeolimnological records, because long-term observations are limited in time and indisputable sediment proxies of hypolimnetic anoxia are still scarce. Here we use visible and near infrared (VNIR), and short-wave infra-red (SWIR) hyperspectral imaging combined with geochemical analyses to reconstruct lake stratification history, redox status and mixing conditions in the water column of Lake Son Kol (Kyrgyzstan) in Central Tian Shan during the last 8500 years. In particular, the detection of Bacteriopheophytin *a* (Bphe *a*), a pigment produced by anoxygenic phototrophic bacteria at the chemocline of meromictic lakes, emphasizes episodes of multi-decadal to centennial hypolimnetic anoxia in Lake Son Kol. Phases of hypolimnetic anoxia are inferred from the deposition of dark organic sediments within a stratified lake system, which occurred during periods of increased snowmelt (and solid winter precipitation) and warmer spring/summer temperatures that promoted floods and the export of terrestrial material from the catchment. Prolonged euxinic conditions in bottom waters (involving the development of a stable chemocline) are reported around 8500, 8400, 8200–7800, 7700–7500, 7300–7000, 6500–6100, 6000–5700 and 5500–5250 cal. yr BP. At ca. 5250 cal. yr BP, the chemocline abruptly vanished as Lake Son Kol tipped into a regime with predominantly cooler and well-mixed conditions (predominance of oxygenic phototrophs), coeval with higher lake levels. The disappearance of hypolimnetic anoxia in Lake Son Kol coincides with strengthened wind conditions that imply enhanced lake overturning and upward mixing of nutrients in the water column. This study reveals the strong potential of hyperspectral imaging, in combination with more classical palaeolimnological approaches, to reconstruct the lake trophic and mixing history and explore the controlling mechanisms at work on decadal to centennial timescales. Our results outline how abrupt ecosystem changes may occur even in the absence of anthropogenic climate change.

1. Introduction

Anthropogenic global warming is changing high-altitude ecosystems and environmental dynamics (Solomon et al., 2007; IPCC 2013). Regional model outputs for Central Asia predict that seasonal surface temperatures in the region will increase from 3 °C up to 11.4 °C on average, coeval with a decline in the amount of precipitation (Ozturk et al., 2012), although uncertainties in hydrological/rainfall projections are existing. High elevation regions of Central Asia (e.g., Tian Shan and Pamirs mountains, Tibetan Plateau) are particularly vulnerable to warmer climate conditions (e.g., Christensen et al., 2007). In high-altitude areas, a consequence of global warming may be shorter and wetter (and milder) winters along with longer and drier summers (Christensen et al., 2007; IPCC, 2013). Increases in solid winter precipitation, spring/summer temperatures, and (summer) rainstorms are likely to increase flooding of snowmelt-fed lake basins. Warmer temperatures are also expected to lead to eutrophication of lakes, depletion of oxygen in deep waters (Jenny et al., 2013), and longer and stronger temperature stratification in summer (e.g., Adrian et al., 1995; Livingstone, 2003; Foley et al., 2012). Incomplete lake overturning may result in the development of a chemocline (Davison, 1993) with an anoxic hypolimnion underneath (Butz et al., 2016), which may last for prolonged periods (meromixis). Meromixis implies persistent lake stratification over multiple years caused by chemical differentiation of the bottom waters, (cf. seasonal thermal stratification which is common in deep temperate lakes and may occur above the chemocline in a meromictic lake). Investigations of long-term trends in oxygen depletion in lakes, and their relationship with climatic changes on timescales beyond the instrumental period, are still scarce in high Central Asia.

Located at the intercept between the influences of the Westerlies and the Siberian Anticyclone (Chen et al., 2008; 2010), the Tian Shan holds key information about past climate variability

and particularly temperature and hydrological changes in western Central Asia (e.g., Rousseau et al., 2020). A number of valuable and high-quality lake sediment studies have examined Holocene climate development in the Tian Shan and Pamir mountains (e.g., Aichner et al., 2015; Beer et al., 2007; Li et al., 2011; Mischke et al., 2010; Chen et al., 2016; Heinecke et al., 2016, 2017, 2018; Rousseau et al., 2020), including several at Lake Son Kol (or Son Kul) in Kyrgyzstan (Huang et al., 2014; Mathis et al., 2014; Pacton et al., 2015; Lauterbach et al., 2014; Schwarz et al., 2017, Wolff et al., 2017; Laug et al., 2020). The focus of these works has been on the Mid- to Late Holocene, with however limited palaeoenvironmental reconstructions between 8500 and 6000 cal. yr BP. Thus there are virtually no high-resolution palaeolimnological records of long-term lake mixing conditions from this region yet, which could provide information on the complex links between environmental, climatic and anthropogenic changes in high-altitude settings.

Here we combine hyperspectral imaging (HSI) and X-Ray fluorescence (XRF) analyses of a new core from Lake Son Kol (SK06) to obtain an unprecedented record of sedimentary pigment changes at ultra-high sampling resolution (μm-scale; sub-annual resolution). Building upon the work of Huang et al. (2014), who inferred that most of the annual precipitation switched from the summer to the cold (winter) season between the Mid- and Late Holocene, we used sedimentary pigments and geochemical data to (i) decipher lake trophic status during the last 8500 years, (ii) investigate when anoxic conditions developed in the hypolimnion, and (iii) assess whether the occurrence of hypolimnetic anoxia can be linked to climatic changes in Central Tian Shan. We further evaluate whether phase boundaries identified in the multi-proxy dataset can be attributed to event-based phase transitions or more gradual shifts using multivariate statistical analyses. Comparisons with other palaeolimnological data from Lake Son Kol and regional records will be used to understand regional climate development in the Tian Shan, as well as implications for lake stratification

dynamics during the Holocene.

2. Study site

2.1. Geological, environmental and lacustrine setting

The geology, geomorphology, climatic and lacustrine characteristics of Lake Son Kol have been extensively studied (Mathis et al., 2014; Huang et al., 2014; Lauterbach et al., 2014). Son Kol (41°50′52″N, 75°07′45″E, 3016 m a.s.l.) is the second largest natural lake in Kyrgyzstan, within the central Tian Shan mountain ranges (Fig. 1). It fills the central depression of an intramontane basin located between two generally east-west stretching mountain ranges, which are the Son Kol Too and Baidula Ranges (3200–3500 m a.s.l.) in the north and the Boor-Albas Range (3800–4000 m a.s.l.) in the south (Shitnikov, 1980). These mountain ranges are composed of Carboniferous sedimentary rocks and Permian granitoids (east and south) and Cambro-Ordovician metamorphic granodioritic and granitic gneisses, as well as strongly folded sedimentary rocks in the north (http://portal.onegeology.org/OnegeologyGlobal/). The modern equilibrium line altitude (ELA) of glaciers at north-facing slopes in the Central Tian Shan is ~3850–4100 m a.s.l., (Narama et al., 2007; Koppes et al., 2008), hence there are no glaciers in the lake watershed today and, based on ELA reconstructions, seem unlikely to have fed Lake Son Kol during the Holocene (Savoskul and Solomina, 1996). The widespread pasture-covered plains surrounding the lake are made up of Quaternary eroded material arranged in old Pleistocene moraines (Abramowski et al., 2006; Narama and Okuno, 2006) and inactive fan deltas. A large fluvial fan-delta nourished by cirque valleys of the Boor Albas range progrades from the southern shore into the lake. Along the southeastern and northeastern shore, large coastal sedimentary features such as sand spits and associated open lagoons have been developed by the prevailing westerly winds, indicating a stable lake level during at least the Late Holocene.

126 Today, Lake Son Kol is located above the treeline, on a high plateau surrounded by mountain
127 meadows. Because of pronounced altitudinal changes over short distances, the vegetation
128 rapidly changes within a few kilometers with the development of a lush alpine meadow in the
129 lake catchment at ~3000 m a.s.l., while conversely steppe to semi-desert environments prevail
130 in open lowlands (below 2000 m a.s.l) with sagebrush steppe (*Artemisia*) and
131 Chenopodiaceae (Mathis et al., 2014).
132 Lake Son Kol is ~29-km long and ~18-km wide, with a surface area of ~275 km^2 and a
133 catchment of ~1130 km^2. The lake water volume is ~2.82 km^3 and the lake is presently ~13-m
134 deep (Lauterbach et al., 2014). According to the lake stratification classifications of Kalff
135 (2002), the depth and climatic location of Lake Son Kol should make it susceptible to shifts in
136 mixing regime. The lake has a single outlet at its southern end, which discharges into the
137 Naryn River and then to the Syr Darya down to the Aral Sea basin. Apart from direct
138 precipitation on the lake surface, most surface inflow is from several small mostly episodic
139 rivers fed by rainfall, groundwater and snowmelt from neighbouring mountains (Huang et al.,
140 2014). A few perennial rivers supply the lake from the west where they braid in a small
141 alluvial plain at the shore. Today, however, most of the inflow is contributed by groundwater
142 (Beloglasov and Smirnova, 1987). Average lake water temperature fluctuates between 16 °C
143 (14.5 °C in summer 2007; Huang et al., 2014) and 0–2 °C in winter, with almost no stable
144 thermal stratification throughout the year (Huang et al., 2014; Lauterbach et al., 2014). Earlier
145 monitoring data reported average summer water temperatures of 12–13 °C (Beloglasov and
146 Smirnova, 1987), with maxima of 20–23 °C during warmer years. Freezing starts in October
147 and ice break-up may begin as early as March (up to late April) depending on short-term
148 climatic variability (Huang et al., 2014).
149 The water column of Son Kol is well mixed and oxygenated to the lake bottom in the
150 summer, though a small oxygen minimum has been noted at a water depth of 1.5 m revealing

151 respiration in the epilimnion (July 2007; Huang et al., 2014). Monitoring data from the 1960s
152 and 1970s similarly reported a well-oxygenated water body throughout the whole year, but
153 Beloglasova and Smirnova (1987) observed oxygen concentrations of 0.8–1.8 $mg.l^{-1}$ or less in
154 the shallow water zone during winter. The strong fetch (maximum effective fetch of ~17 km;
155 Håkanson et al., 1983) and the high wind frequency (wind speeds up to 20 $km.h^{-1}$ in summer
156 and fall) impart efficient and complete mixing of the shallow water body. According to
157 previous surveys the weather is calm only during 11% of the ice-free season (Beloglasov and
158 Smirnova, 1987). In line with this, surface/intermediate flow currents reaching 2–8 $cm.s^{-1}$
159 across the water body (and up to 10 $cm.s^{-1}$ in the deepest part of the basin) reflect a highly
160 dynamic lacustrine system (Beloglasov and Smirnova, 1987). Such conditions guarantee for a
161 steady mixing of the whole water column and thus makes Son Kol mostly a polymictic lake
162 nowadays (apart from under ice in winter). Son Kol is a moderate hard-water lake (4.56–4.96
163 mg^{-1}) with a mineralisation of 465 $mg.l^{-1}$ (summer) and 306 $mg.l^{-1}$ (winter) (Beloglasov and
164 Smirnova, 1987). Accordingly, today it is a bicarbonate lake with weak magnesium
165 dominance. Conductivity throughout the water column ranged between 515 and 530 $mS.cm^{-1}$
166 in the summer of 2012 (Schwarz et al., 2017).
167
168 *2.2. Climatic setting*
169 Local climatic conditions lead to short temperate summers and severe cold winters, with snow
170 cover between November and April. Mean annual air temperature is -3.5 °C (mean of 11 °C
171 in summer and -20 °C in winter), based on the nearest meteorological station (Dolon, 41.8° N,
172 75.8° E, 3040 m a.s.l.) (Shnitnikov, 1980). Mean annual precipitation is 500–600 mm at Lake
173 Son Kol, with a maximum in summer and a minimum in winter (Academy of Science of the
174 Kyrgyz SSR, 1987). The current precipitation regime in the Tian Shan Mountains
175 surrounding Son Kol is mainly regulated by the interaction between cyclonic activity driven

176 by the mid-troposphere Westerlies and the southwestern branch of the Siberian anticyclonic
177 circulation (Aizen et al., 1997). Atmospheric dust concentrations (and loess) are maximal
178 below 3000 m a.s.l in Central Asia, with thickest loess accumulations occurring between 1000
179 and 1300 m a.s.l in the piedmont regions of the Tian Shan (Machalett et al., 2008). Different
180 airflows govern convective surface winds in western Central Asia and thus, the regional
181 distribution of remote dust particles over the year (Bugaev et al., 1957; Shettler et al., 2014).
182 During the summer northwestern, western and northern air intrusions and northeast
183 anticyclonic flows control up to 83% of the local wind directions. Dust monitoring near
184 Bishkek reveals besides that wet deposition is a substantial process for aerosol deposition in
185 mountain areas (Shettler et al., 2014). Nonetheless, backwards trajectories calculated from
186 Son Kol document that remote air masses likely also come from southern (Afghanistan) and
187 further western (Mediterranean) and northern (North Atlantic) sources (Shettler et al., 2014).
188
189 **3. Material and methods**
190 *3.1. Lake coring and cross-core correlation*
191 Four sediment cores, including two sets of parallel cores, were extracted with a Uwitec piston
192 corer in July 2007 from two different sites in the southeastern part of Lake Son Kol (Fig. 1).
193 Core SK04 (133cm) was obtained at ca. 1.15 km from the southern shore (41°46'56.6"N,
194 75°08'18.2"E, 10.5 m water depth) while a second set of parallel cores, SK06 and SK07 was
195 retrieved at 1.6 km northeast of core SK04 (41°47'45.2"N, 75°08'22"E, 12.5m water depth)
196 (Fig. 1). Although cores SK04 and SK07 have been extensively analyzed recently (Mathis et
197 al., 2014; Huang et al., 2014; Pacton et al., 2015), no integrative study has been undertaken on
198 core SK06 yet, although it represents the longest lacustrine archive ever retrieved in Lake Son
199 Kol. In spite of the significant distance between the two coring sites, the cores exhibit very
200 similar sedimentary successions (and lithological marker layers), thus allowing a robust core-

to-core correlation (Fig. 2a), as also demonstrated by the good match between magnetic susceptibility records for cores SK04, SK06 and SK07 (Fig. S1). Core SK06 was split in half lengthwise and photographed directly after core opening. A detailed macroscopic description established the different sedimentary facies (Units I-VI) as well as the stratigraphic correlations between cores SK04, SK06 and SK07 (Fig. 2a). No compaction and/or disturbance was observed in SK06.

3.2. Age-depth model

Owing to the robust core-to-core correlation between cores SK06, SK04 and SK07 (Figs. 2 and S1) and SK06 and SONK_11_D1/2 from Lauterbach et al. (2014) (Fig. S2), the chronology of core SK06 (Fig. 2b) was established using available radiocarbon (AMS ^{14}C) dating of both terrestrial plant macroremains and bulk sediment organic matter (OM), complemented by one short-lived radionuclide measurement (^{241}Am). We selected and reappraised 8 bulk sediment samples and one terrestrial leaf from cores SK04 and SK07 (Huang et al., 2014) along with one terrestrial plant remains from core SONK_11_D1/2 (Lauterbach et al., 2014) (Table 1). ^{14}C age anchor points were transferred to core SK06 using a detailed correlation of both lithological marker layers and magnetic susceptibility between core SK06 and SK04 and SK07 (Figs. 2a and S1) and between cores SK06 and SONK_11_D1/2 (Fig. S2). For the latter, the correlation at 33 cm in core SK06 of Poz-44073 date (at 33 cm in SONK_11_D1/2; Lauterbach et al., 2014) is a robust anchor point for the core SK06 chronology, making the Poz-26363 radiocarbon age at 30 cm too old, and so this date was rejected from the age model. Note that not all the radiocarbon ages reported in Huang et al. (2014) were applied to core SK06 by cross-core correlation, since we only rely on age points that could be confidently transferred to core SK06. Poz-26363, Poz-26370 and Poz-26372 dates were rejected because they imply the reworking of older material in younger

sediments. Poz-37470 date (bulk sediment organic matter) was not used either because a terrestrial leaf dated in the same stratigraphic level was preferred (Poz-37469). Other discarded ages correspond to depths that could not been matched properly between cores SK04 and SK06 (Poz-26368).

A 150-yr reservoir age correction was further applied prior to calibration to each transferred conventional radiocarbon age by using the 155 ± 30 ^{14}C yr BP reservoir age obtained on live deep-water algae by Lauterbach et al. (2014) (Table 1). Such a small reservoir age offset implies that the recent hardwater effect is small; this is further confirmed by nearly identical radiocarbon ages (within error bars) obtained on one bulk organic sample (not used here) and a terrestrial leaf from the same stratigraphical level in core SK04 (see Table 1 and Huang et al., 2014). More detail regarding reservoir effects in Lake Son Kol is provided in Lauterbach et al. (2014).

In order to constrain the age of the topmost sediments in core SK06, we used the close agreement of lithological markers in cores SK06 and SONK_11D1/2 and assumed that the notable increase in ^{241}Am activity at 5.5 cm in SONK_11_D1/2 occurs at 2 cm in core SK06 (Fig. S2), and corresponded to the Northern Hemisphere nuclear weapons testing maximum in 1963 CE (Appleby et al., 1991). The topmost ca. 2 cm of SONK_11_D1/2 are missing in core SK06. Finally, the age-depth model for core SK06 was established using 10 corrected conventional radiocarbon ages (Table 1), as well as the ^{241}Am anchor point at 2 cm sediment depth (most likely 1963 CE), as input parameters for a *P_Sequence* deposition model implemented in Oxcal 4.4 (Ramsey, 2008) (Fig. 2b). The *k* parameter was set to 1 (as in Huang et al., 2014) and the radiocarbon ages were converted to calendar years by using the IntCal20 terrestrial calibration curve of Reimer et al. (2020). The high agreement index A_{model} of 89.8% indicates that the chronology of core SK06 is reliable (Ramsey, 1995; 2001).

3.3. Geochemistry

Major elements in the sediments were measured by XRF at high-resolution (500-µm step size) on the split-core surface with an Avaatech Core Scanner (EDYTEM Laboratory). Prior to measuring, the core surface was cleaned and foiled to prevent contamination and core desiccation. The X-ray beam was generated with a rhodium anode and a 125-µm beryllium window, which allows a voltage range of 7–50 kV and a current range of 0–2 mA. Geochemical data were obtained with different settings according to the elements analyzed. They were adjusted at 10 kV and 1 mA for 10 s to detect Si, Ca, Al, Fe, Ti, K, Mn and S. For heavier elements (i.e., Sr, Rb, Zr, Br and Pb), measurements were performed at 30 kV and 9.75 mA for 30 s. XRF data are displayed as element intensities in count per second (cps) (Fig. S3). Because no major element concentration was conducted on core SK06, we rely here on XRF core-scanner data available on core SK07 (unpublished data) in order to calibrate XRF measurements in core SK06. Major element concentrations on core SK07 were previously measured on 1.5-cm thick discrete samples using XRF at the University Lyon1. The sampling was conducted at a step of about 3–5 cm to allow for one calibration measurement every 3–5 core scanner measurement in core SK07.

3.4. Hyperspectral imaging

Hyperspectral imaging is a visible and near infra-red spectroscopic method measuring the reflectance of the sediment surface exposed to an incident light, and thus the sediment composition (Barranco et al., 1989; Balsam and Deaton, 1996; Balsam et al., 1997). Prior to analysis, the thin, superficial layer was scraped from the sediment to ensure a uniform surface. Reflectance spectroscopy was performed on a core logger bench equipped with two hyperspectral cameras (VNIR-PFD and SWIR, SPECIM®), which offers a short sampling time and allows for high spatial resolution (several dozens of µm; Jacq et al., 2020). The

distance between the studied sample/core and the camera lens was 130 mm, with an acquisition angle of 90°. The surface of the sediment is indirectly illuminated by 18 halogen bulbs homogeneously distributed around the lens. The acquisition speed of the core logger was 0.5 $mm.s^{-1}$. Pixels in the resulting Visible and Near Infrared (VNIR) image each cover an area of 47×47 μm^2 and contain raw spectral data from 400 to 1000 nm at 6.5 nm spectral resolution (given in digit number, DN), whereas the Short Wave-Infrared (SWIR) image pixels have a resolution of 150×150 μm^2 and cover a spectral range from 1000 nm to 2500 nm at 10 nm spectral resolution. Therefore, each pixel contains spectral information related to sediment composition. The depth of field of the imagers is ca. 2 mm. A normalization step is required to convert raw data (8 bits) to % reflectance. At each acquisition, a 100% reflective SPECTRALON standard was measured and used as a reference to express the data as % reflectance. Data processing was carried out with the ENVI (v. 5.3) and IDL 8.0 softwares. Pigment composition and concentrations were inferred from area indices (Fig. 3), which directly measure the surface area (here referred to as relative absorption band area or RABA; Trachsel et al., 2010) between the continuum and the reflectance spectrum at the absorption band targeted (for instance for the chlorophyll-a and its derivatives at 670 nm). The sum of the reflectance bands located throughout the absorption band is subtracted from the area under a line connecting the beginning and the end of the depression formed by the absorption band. In this study, area indices are followed by wavelengths indicating the width of the absorption band considered (e.g. RABA630-700). The main absorptions are determined by continuum removal, which also allows estimating the most interesting wavelength interval. In this study, we have defined four of them centered on 670 nm, 615 nm, 844 nm and 1670 nm (Fig. 3).

3.5. Coprophilous fungal spore analysis

Catchment erosion processes in high-altitude landscapes may be re-shaped by livestock grazing related to pastoral activity (Giguet-Covex et al., 2011). The variability of grazing pressure and associated soil erosion in a catchment area can be reconstructed from the sedimentary abundance of coprophilous fungal ascospores in lake sediments, as a proxy for the density of wild and domestic herbivores (Davies and Schaefer, 2006; Gauthier et al., 2010; Etienne et al., 2013). Son Kol catchment is still an area of transhumance today; therefore, domestic herbivores are assumed to be the primary source of coprophilous fungal spores in lake sediments, and wild herbivores are regarded to be a trivial source. To evaluate the impact of grazing activity on soil erosion in the catchment, abundances of coprophilous fungi ascospores were measured in 37 samples of core SK06 (for the last 6000 years). The resolution is approximately 100 years from 6000 to 5000 cal. yr BP, and about 250 years from 5000 to 1500 cal. yr BP. Samples were chemically prepared according to the procedure of Faegri and Iversen (1989). *Lycopodium clavatum* tablets (averaging 20,848 spores per tablet) were added to each sample (Stockmarr, 1971) to express the results as influx or accumulation rates (number.cm^{-2}.yr^{-1}). Coprophilous ascospores were identified and counted using a photonic microscope following pictures and descriptions in van Geel and Andersen (1988), van Geel et al. (2003), Van Geel and Aptroot, 2006, Feeser and O'Connell (2009), Cugny et al. (2010) and Gelorini et al. (2012). Total coprophilous fungi *sensu stricto* include *Delitschia* (UG-1066), *Neurospora* sp. (HdV-1), *Podospora*-type (HdV-368), *Sordaria*-type (HdV-55A), *Sporormiella* (HdV-113), and *Trichodelitschia* (HdV-546).

3.6. Data analysis

Linear dimension reduction was performed by applying a correlation matrix-based principal component analysis (PCA) using the PAST v. 4.02 software (Hammer et al., 2001). The PCA was supplied with XRF (major elements) and hyperspectral data from core SK06 (Fig. 4).

Due to very high levels of non-normality and heteroscedasticity of the original descriptors, data were first log-transformed and then separately centered on a per-sample basis in order to remove overall-count effects and to focus on relative variations among samples. Also using the PAST software, time series corresponding to the resulting PC1 and PC2 were further investigated using Gallagher et al.'s (2011) Bayesian "changepoint modeling" algorithm for identifying abrupt regime shifts in time series, often referred as tipping points in geosystems (Lenton et al., 2008; Lenton, 2011; Scheffer et al., 2012). Number of MCMC iterations required by Gallagher et al.'s method was set to 1,000,000 with a burn-in phase of 20,000 iterations; up to 300 changepoints were allowed a priori in order to generate fully-unconstrained changepoint models, resulting in an average number of changepoints of 74 and 61 for the PC1 and PC2 time series, respectively.

4. Results and interpretation

4.1. Sedimentology

Sediments mostly consist of alternating yellowish and light-brownish calcareous muds in the upper 1.22 m of core SK06, whereas dark organic-rich muds alternating with yellow-brown calcareous muds and white carbonate layers predominate between 1.22 and 1.91 m (Fig. 2). The transition between the basal organic-rich sediments and the upper 1.22 m alternating calcareous muds is characterized by homogeneous greyish calcareous clays between 0.94 and 1.22 m. Apart from this transition, the sediments are finely laminated in core SK06, and especially in dark organic sediments. XRF core scanning data allows deciphering the distinct geochemical composition of the three main lithologies (Fig. S3). Dark organic sediments are typified by their high abundances in Br and S (Figs. S3 and 5), whereas the intervening carbonate layers exhibit an enrichment in Ca and Sr (Fig. S3). In contrast, the transition interval (greyish homogenous clays) is best described by high abundances of Ti, Rb, Zr, Fe

and Si, emphasizing their high mineral content. The upper alternations between yellowish and light-brownish sediments are characterized by a mixed geochemical composition and exhibit fluctuating values of Ti, Rb and Zr, but also highly variable abundances of Ca and Sr (Fig. S3).

4.2. VNIR-SWIR proxy data

Chlorophyll *a* (Chl *a*) and its derivative products (Rein and Sirocko, 2002; Das et al., 2005; Wolfe et al., 2006; Michelutti et al., 2010) was measured as the area index between 630 and 700 nm (RABA630–700) normalized by the absorption maximum at 670 nm (R_{670}) (Fig. 3) as defined by Wolfe et al. (2006). Although Chl *b* may contribute in the absorption range between 630 and 700 nm (i.e., at 652 nm, Bidigare et al., 1990; Yacobi et al., 2015), it is not observed in our spectral data (Fig. 3). We therefore assume that the measured absorption peak of particles at 670 nm almost exclusively represents the optical activity of Chl *a*, apart from the slight interference by the accessory chlorophylls Chl *b* and Chl *c*.

Phycocyanin is a water-soluble accessory pigment to chlorophyll exhibiting a notable absorbance trough around 610–620 nm for C-phycocyanin (Glazer et al., 1973; Yacobi et al., 2015). For this study, we propose to screen the phycocyanin content by measuring the area index between 600 and 630 nm (RABA600–630) normalized by the absorption peak at 615 nm (R_{615}) as described by Yacobi et al. (2015) (Fig. 3). It must be recalled, however, that the absorption of Chl *a* and accessory chlorophylls Chl *b* and Chl *c* partly overlap the range of optical activity of phycocyanins, although weakly (Yacobi et al., 2015). However, the RABA630-700 and RABA600-630 curves exhibit different patterns (Fig. 5), implying that a genuine signal does exist apart from the Chl *a* plus derivatives. This also suggests that phycocyanin predominates in some intervals where Chl *a* plus derivatives do not (Fig. 5), thus allowing their respective trends to be distinguished and analyzed separately in core SK06.

375 Phycocyanins are common in cyanobacteria (Williams et al., 1980), and their concentration in
376 shallow lacustrine systems is used to estimate the presence and relative abundance of
377 cyanobacteria (Horváth et al., 2013). Phycocyanin has been reported in lacustrine sediments
378 of Lake Qinghai, Central China (Ji et al., 2009) and used to indicate cyanobacterial blooms in
379 the Baltic Sea (Woźniak et al., 2016). Chl *a* plus derivatives and phycocyanin contents are
380 thus interpreted here as a proxy for oxygenic phototrophs, which usually indicate aerobic
381 conditions. Total Bacteriopheophytin *a* (Bphe *a*) is a stable degradation product of
382 Bacteriochlorophyll *a* or Bchl *a* with a characteristic spectral absorbance in the infrared range
383 around 750–770 nm in ethanol extracts (Coolen and Overmann, 1998; Rogozin et al., 2012)
384 and 800–900 nm in sediments (Scheer, 2006; Ji et al., 2009; Blankenship, 2013). Bphe *a* was
385 determined from the area index between 750 and 900 nm (RABA750–900) normalized by the
386 absorption maximum at 844 nm (R_{844}) as defined by Butz et al. (2015) (Fig. 3). Because no
387 other known bacterial pigment absorbs at this wavelength, the relative abundance of Bchl *a*
388 (and its derivative by-products Bphe *a*) can be evaluated by measuring the Bphe *a* absorption
389 trough between 750 and 900 nm normalized by the absorption peak at R_{844}. Although
390 Bacteriopheophytin *b* (Bphe *b)* may also contribute at 820 nm (Oren, 2011), no absorption
391 peak is observed at that wavelength in our data (Fig. 3). We therefore assume that the
392 measured absorption peak of particles at 844 nm represents exclusively the optical activity of
393 Bphe *a*. Bphe *a* is produced by planktonic anoxygenic phototrophic bacteria (APBs) such as
394 purple sulphur bacteria (Chromatiales, Rhodospirillales; Schmidt et al., 2002; Rogozin et al.,
395 2012) which commonly live in the chemocline of stratified meromictic lakes, where reduced
396 sulphur species are very abundant and oxygen levels are low, if sufficient light is available for
397 photosynthesis (Butz et al., 2016). Hence Bphe *a* is a diagnostic pigment for photosynthesis
398 in anaerobic conditions and the presence of that pigment in the sediment may help infer long-
399 term lake stratification, and the presence of a chemocline (Fig. 5). Aromatic organic matter

content (ARO) has a characteristic absorption near 1670 nm (Wheeler, 1959) and it seems that no other compound absorbs at this wavelength, so we assume that an index in this spectral range can infer this property (Fig. 5). Nevertheless, we are aware that SWIR measurements may be influenced by sediment moistness and grain size, for which no known correction can be applied yet. For this study we propose the area index between 1660 and 1690 nm (RABA1660–1690), normalized by the absorption maximum at 1670 nm (R_{1670}). ARO values are interpreted as a proxy for tracking the inputs of terrestrial organic matter from the shore (e.g., soils) and related catchment, with high (low) ARO corresponding to increased (decreased) inputs of detrital organic matter.

4.3. PCA analysis

XRF and hyperspectral (VNIR, SWIR) data, with a temporal resolution ranging between 3 $yr.mm^{-1}$ and 7–8 $yr.mm^{-1}$, were jointly analyzed by PCA in order to characterize sediment end-members and detect abrupt shifts in the multivariate time series (Fig. 4a). The XRF core-scanner of Ca, Fe and Ti was previously calibrated using XRF conducted on discrete samples in core SK07 (28 samples), exhibiting an excellent match between the two methods (Fig. 4b). PC1, PC2 and PC3 together explain about half of the total variance (Figs. 4a and S4), allowing for the identification of different end-members in the lake system: (i) high Ti, Rb, Fe and RABA1660–1690 values for PC1 > 0 (which are related to organic and minerogenic inputs from the catchment), while Sr, Ca (which indicate endogenic carbonate precipitation) and to a lesser extent Zr (coarse detrital input) drive PC1 < 0, making PC1 a proxy for allochthonous vs autochthonous products in the lake system; (ii) high Mn, RABA600–630 and RABA630–700 values for PC2 > 0 (which are related to oxic conditions in the water column) vs. high Br, S (and to a lesser extent Zr) and RABA750–900 values (which are linked to organic matter content and infer reducing and sulphidic conditions in bottom waters)

425 for PC2 < 0, making PC2 a proxy for oxygenated vs. euxinic bottom water conditions in Lake
426 Son Kol. Based on this result, prominent environmental change occurred around 8400, 8200–
427 7800, 7700–7500, 7300–7000, 6500–6100, 6000–5700 and 5500–5250 cal. yr BP (Fig. S5),
428 when increased influx of detritus (PC1 > 0) is in close correspondence with the development
429 of euxinic conditions in the hypolimnion (and thus of a chemocline; PC2 < 0). The Si content
430 appears to slightly differ from other terrigenous (river-borne) elements (PC1 and also PC3
431 [14.4%], whose palaeoenvironmental signature is more difficult to interpret and is not
432 discussed here) (Fig. S4). Si-value is high in the silt fraction and is, in addition to its weak
433 riverine contribution, mostly linked with aeolian inputs into the lake (Huang et al., 2014).
434 Judging from the lack of any conspicuous link to the other elements (Fig. 4a) and given the
435 biochemical reactivity of this element, Mn is used to decipher bottom-water redox processes,
436 as already reported in other lacustrine settings (Wirth et al., 2013; Davies et al., 2015).
437
438 *4.4. Time series of hyperspectral and geochemical data*
439 Between 8500 and 7000 cal. yr BP (191–164 cm), phycocyanin (from cyanobacteria) has the
440 highest abundances downcore, probably related to the development of benthic cyanobacterial
441 mats in a shallow water body (Fig. 5). Chl *a* plus derivatives and Bphe *a* also oscillate at very
442 high frequency. Bphe *a* and ARO maxima occur repeatedly around 8500, 8400, 8200–7800,
443 7700–7500 and 7300–7000 cal. yr BP, corresponding to dark organic-rich sediments along
444 with high Br and S content. No match was found, however, between phycocyanin and Chl *a*.
445 Subsequently, Chl *a* plus derivatives and phycocyanin exhibit a pronounced decline between
446 7000 and 6500 cal. yr BP. Phycocyanin abundances drop from 7000 cal. yr BP onwards and
447 never recover to former levels. Bphe *a* and ARO values also exhibit a drastic decrease in this
448 time interval, as also do Br and S content.

From 6500–5250 cal. yr BP, Chl *a* plus derivatives values increase and reach their highest abundances downcore, with however considerable fluctuations. Bphe *a* content recovers to high levels and even dominates between 5750 and 5250 cal. yr BP, but dramatically decreases and readily disappears from 5250 cal. yr BP onwards (Fig. 5). Coevally, Br, S and ARO values are also high between 5750 and 5250 cal. yr BP (corresponding to the deposition of dark organic sediments), but rapidly drop after 5250 cal. yr BP. Chl *a* plus derivatives and phycocyanin exhibit a prominent decline in their abundances between 5000 and 3850 cal. yr BP. Judging from XRF core-scanner data, enhanced detrital inputs occurred in this interval (Fig. S3). Subsequently, Chl *a* plus derivatives and phycocyanin increase from 3850–3100 cal. yr BP, whereas Bphe *a* still oscillates at very low levels. Higher Br, along with enhanced ARO, also parallels the occurrence of dark organic-rich sediments in this interval. Over the course of the last 3000 years, oxygenic phototrophs fluctuate at lower levels, whereas Bphe *a*, Br and ARO remain low (Fig. 5).

4.5. Abrupt regime shifts

Abrupt regime shifts were identified based on slope variations of the average changepoint model calculated separately for PC1 and PC2. For each principal component, average changepoint model's slope (absolute value) is plotted against time, with 99% and 95% percentiles taken as cut-off values (Figs. 6 and 7). Time intervals with average changepoint model's slope values above these cut-offs indicate abrupt changes in the time series, and can therefore be regarded as tipping points. For PC1, tipping points are recognized as 10–20 yr intervals (beyond the 99% percentile value) at ca. 3670, 5050–5080 (highest slope value), 5250, 5370, 5850, 6150, 6220, 6900, 7030, 7980, 8230, 8280 and 8340 cal. yr BP (Fig. 6). For PC2, tipping points are similarly identified as 10–20 yr intervals (beyond the 99% percentile value) around 5250 (highest slope value), 5950, 6040, 6230, 6280, 6380, 6670,

6700, 6900, 7060, 7750, 7800, 8320 and 8380 cal. yr BP (Fig. 7). Hence the time intervals around 5050–5250, 6220–6240 and 8200–8400 cal. yr BP are detected for both PC1 and PC2, and probably correspond to abrupt regime shifts in the lacustrine system. Interestingly, low PC2 values match with a strong peak of magnetic susceptibility (Figs. S1 and S5) around 8200–8400 cal. yr BP, suggesting the occurrence of abrupt changes in the lake and surrounding catchment that are tied with the 8200 cal. yr BP cold event widely recognized in the Northern Hemisphere (Alley et al., 1997; Rohling and Pälike, 2005).

5. Discussion

Between ca. 8500 and 5250 cal. yr BP anaerobic conditions (and the penetration of light deep in the lake to support photosynthesis for APB) are inferred from high Bphe *a* and Br (PC2 < 0), along with the occurrence of dark organic layers (Fig. 5). Coevally, high ARO and minerogenics content (PC1 > 0) suggest enhanced inputs of detrital organic matter and a link between terrestrial influx, sedimentary dynamics and the advent of hypolimnetic anoxia in the earlier part of the record. After 5250 cal. yr BP, the near absence of Bphe *a*, lower ARO values but persistently high abundances of oxygenic phototrophs suggest prolonged aerobic conditions within a well-mixed water body (Fig. 5).

5.1 Episodes of increased snowmelt and indicators of lake-level changes

Grain size and geochemical/isotopic (TC, TN, TOC, C/N, $\delta^{13}C_{org}$ and $\delta^{18}O$) data can be useful in supporting interpretations from hyperspectral and XRF data. Here we compare previously unpublished and available data from SK07 (Huang et al., 2014) to help interpret the 8500–5000 cal. yr BP time interval during which dark organic intervals are recurrently interbedded with yellow-brown calcareous muds (Fig. 7). Altogether, these parameters help to distinguish

498 changes in onshore and in-lake environmental conditions such as sheet-wash from the shore,
499 productivity and nutrient availability, and the possible mechanisms at work.
500 Generally, the timing of changes in geochemical and isotopic proxies in core SK07 agree with
501 those of XRF and hyperspectral data from core SK06 (Fig. 8). Dark organic intervals with Br
502 and ARO in core SK06 have elevated TOC, TC, TN and C/N values but strongly depleted
503 $\delta^{13}C_{org}$ and $\delta^{18}O$ values in core SK07. Such prominent $\delta^{13}C_{org}$ depletions might indicate the
504 predominance of APB during phases of lake stratification because pronounced carbon isotope
505 fractionation towards lighter $\delta^{13}C$ has been associated with purple sulphur bacteria in
506 meromictic lakes (Zyakun et al., 2009). Alternatively, short-lasting depletions in $\delta^{18}O$ can
507 indicate seasonal shifts in the hydrological regime; i.e., increased winter precipitation and/or
508 increased meltwater discharges linked to erosive runoff during spring snow thaw, but also
509 increased temperatures (Huang et al., 2014; Lauterbach et al., 2014) that would have fueled
510 meltwater runoff. The dark organic-rich and $\delta^{18}O$-depleted intervals co-occur with coarser
511 (e.g., silt- and sand-sized) minerogenic and organic (e.g. phytoclasts) inputs into the lake
512 (Figs. 8 and S6), whereas the intervening yellow-brown calcareous muds are enriched in finer
513 (clay-sized) detritus with low sand content (Fig. 8). Erosive runoff after thawing during spring
514 (Huang et al., 2014), and/or higher winter snowfall (Lauterbach et al., 2014), can account for
515 coarse detritus discharge into the lake. Interestingly, the PCA analysis reveals that higher
516 detrital inputs (PC1 > 0) are not associated with elevated Zr content in core SK06 (Fig. 4);
517 instead, dark organic layers exhibit low Zr content (Figs. 8 and S3). Zr is usually more
518 concentrated in sand-size lacustrine sediments (e.g., Cuven et al., 2010; Davies et al., 2015)
519 and so, this Zr depletion in a few coarse dark organic intervals is puzzling, since otherwise all
520 detritics (Ti, Rb and Zr) exhibit similar trends in the intervening yellow-brown calcareous
521 muds (Fig. S3). Therefore, enhanced levels of Ti and Rb along with lower Zr (thus PC1 > 0)
522 in the Br-enriched (PC2 < 0) dark organic layers either suggest the dilution of Zr input by Ti-

and Rb-laden terrestrial organic matter delivered during snow thaw (as inferred from high ARO values), and/or the dilution of Zr (associated with the coarse detrital fraction) during relatively high lake water level phases. Zr mainly originates from erosion processes in the upper catchment of Lake Son Kol because Zr is abundant in local Paleozoic intrusives (granites and granodiorites), but these tend to be covered by Quaternary sediments and soils (colluvial and glacifluvium deposits) on the shoreline belt and further up-valley. Although Zr is linked to Br and S on PC2, Zr is also significantly associated with elevated Sr and Ca (PC1 < 0; Fig. 4), suggesting that Zr is enhanced during low lake water levels, which promotes endogenic carbonate precipitation (Huang et al., 2014). Hence higher Zr infers the increasing influence of riverine discharges at relatively low lake levels and the reduced distance between the coring site and proximal detrital sources. Dilution of Zr most probably occurs during short-lived increases in lake levels, which in turn enhance the formation of organic-rich deposits in Lake Son Kol when elevated terrestrial inputs from snowmelt strengthened the export of dissolved organic matter into the lake. The most probable sources of material during snowmelt discharges (e.g., floods) are the abundant fan delta/fluvial material at the southern edge of the lake, and/or superficial sediments on the slopes (e.g., colluvium) directly adjacent to Lake Son Kol. In contrast, higher Ti, Rb and Zr occur coevally during lower lake level phases, which correspond to the deposition of grey calcareous muds enriched in fine siliciclastics (Fig. S3). Hence higher Zr, Sr and Ca values indicate lower lake water levels and coincide with the deposition of yellow-brown calcareous muds. In contrast, dark organic deposits enriched in Br, S, C/N and TOC are associated with the injection of large volumes of sediment-laden sheet-wash from the shores (high ARO values) during intensified winter precipitation and/or stronger snowmelt (Huang et al., 2014; Lauterbach et al., 2014), which are likely to occur under warmer climate conditions.

548 *5.2. Redox conditions and oxygenation of the hypolimnion*

549 The geochemical behavior of Mn-enriched phases can be used to infer past redox conditions
550 and thus help diagnose oxic and sulphidic redox regimes in the water column (Fig. 9), as
551 reported from Lake Cadagno (Wirth et al., 2013). Based on elevated Mn content, oxic
552 conditions (PC2 > 0) prevailed around 8300–8200, 7400–7250, 5500–5400 and in particular
553 between 5000 and 3800 cal. yr BP in Son Kol when Mn was flushed to the lake with detrital
554 input, and probably occurred in the water column as dissolved unstable Mn^{2+} or as oxidized,
555 particulate Mn-(oxyhydr)oxides. However, no Mn-(oxyhydr)oxides were found in SK06,
556 possibly due to a reduction of Mn^{2+} (leading to a further recycling of Mn into the water
557 column) if the sediment-interface and/or the sediments were reducing. Oxic water column
558 conditions were accompanied by the precipitation of various carbonate minerals judging from
559 the regular occurrences of carbonate layers (Pacton et al., 2015), as well as high XRF-Ca
560 content in the yellow-brown calcareous muds separating dark organic-rich sediments, thus
561 reflecting the high alkalinity of lake waters during those time intervals. The regular
562 occurrence of sediment-dwelling ostracods and molluscs (which require well-oxygenated
563 bottom waters) further supports that a well-mixed (polymictic) water body, with oxic bottom
564 waters, has been established during the last 5000 years (Huang et al., 2014), in accordance
565 with recent monitoring data (Lauterbach et al., 2014).

566 In contrast, there is compelling evidence that the hypolimnion recurrently turned to a
567 sulphidic (euxinic) redox regime between 8500 and 5250 cal. yr BP, involving a stabilization
568 of the water-column stratification and the full development of a chemocline. Low sedimentary
569 Mn concentrations (Fig. 9), the absence of carbonate phases and the drastic increases in Br
570 and S content (PC2 < 0) characterize several phases of euxinic bottom waters between 8500
571 and 5250 cal. yr BP. Coevally, high Bphe *a* values (inferring that purple sulphur bacteria
572 thrived in the water column), and the rising TOC content in dark organic-rich sediments (Fig.

8), are good indicators of reducing bottom water conditions. Although such a hypothesis was ruled out by Lauterbach et al. (2014) based on the absence of varves and/or vivianite crystals (the latter indicating anoxic conditions in a non-suphidic environment during sediment deposition, which is obviously not the case here) in dark organic-rich sediments, several lines of evidence advocate for the recurrence of hypolimnetic euxinia (and thus the development of a chemocline) in Lake Son Kol before 5250 cal. yr BP. Prolonged lake stratification and reducing oxygen conditions around 8500, 8400, 8200–7800, 7700–7500, 7300–7000, 6500–6100, 6000–5700 and 5500–5250 cal. yr BP (Fig. 9) are inferred from (1) high TOC contents (up to 16%) in dark organic-rich layers (Fig. 8) that imply both reducing bottom water conditions which prevents organic matter degradation and especially of photosynthetic pigments (Figs. 7 and 9); (2) the unusual preservation of numerous colonies of coccoid prokaryotes altogether with the preserved intracellular content of cyanobacteria that requires anoxic conditions (Pacton et al., 2015) and in particular, (3) the regular occurrence of Bphe *a* pigments that indicate photosynthesis in anaerobic conditions and thus hypolimnetic anoxia between 8500 and 5250 cal. yr BP.

5.3. Origin and driving mechanisms of detrital-rich organic layers in Lake Son Kol

As developed previously, the onset of euxinic bottom water conditions in Lake Son Kol between 8500 and 5250 cal. yr BP most likely occurred under warmer climate conditions that fostered meltwater runoff. Climate warming possibly fostered permafrost melting, which activated the subaquatic springs that in turn fed the lake with solute-rich waters. Such conditions are highly favorable for the sustainment of stable lake stratification and the development of a chemocline, as observed in other high-altitude lake settings (Wirth et al., 2013). However, this seems to be inconsistent with the regular occurrence of coarse material in dark organic-rich sediments, which implies the transport of organic and minerogenic

599 detritus over long distances in Lake Son Kol. In meromictic lakes, the deposition of coarse
600 detritics in a coring site today located more than 3 km from the shore could be attributed to
601 hyperpycnal or mesopycnal currents (Mulder and Chapron, 2011), depending on the density
602 contrast between inflowing and lake waters. Hypopycnal flows are not considered here
603 because hypopycnal flows in lakes generally supply small quantities of sediments and would
604 require further reconcentration processes in the lake (over a 3-km distance in the case of Lake
605 Son Kol). Aeolian deposition of coarse-grained detritics (including large phytoclasts, Fig. S6)
606 is unlikely as we would expect much finer grain sizes in the case of loess deposits (i.e., silts)
607 (Huang et al., 2014), and loess deposits are generally restricted to lower altitudes in the
608 piedmont of the Tian Shan Mountains (Machalett et al., 2006; Lauterbach et al., 2014).
609 Finally, increased coastal wave erosion driven by winds can be rejected as well because
610 higher wave activity would also have broken down the chemocline. Moreover, hyperpycnal
611 deposits are often typified by sharp-based lag rich in organic debris (Mulder and Chapron,
612 2011), which is never encountered in core SK06 where coarse detritics are rather
613 homogenously distributed in the organic-rich layers (apart from the occurrence of a few
614 normal graded beds; Fig. S6). Hence, the most reasonable candidates for the deposition of
615 coarse minerogenic and organic detritus at the coring site are homopycnal or mesopycnal
616 flows. Homopycnal flows result from a small density contrast between the entering flow and
617 the surrounding water (Bates, 1953) and can export suspended sediment load either in
618 stratified of non-stratified lake basins (Mulder and Chapron, 2011). Alternatively, mesopycnal
619 flows are partially buoyant mesopycnal flows (interflows) of turbid plumes forming along
620 each pycnocline (that separates each water mass) (Van Rensbergen et al., 1998, 1999;
621 Schröder et al., 1998; Chapron et al., 2004, 2005; Støren et al., 2010; Mulder and Chapron,
622 2011).
623

624 Formation of mesopycnal currents is promoted when the inflowing waters enter more saline
625 lake waters, as occurred between (at least) 6000 and 5000 cal. yr BP when higher
626 conductivities (very low lake levels) were inferred in Lake Son Kol (Schwarz et al., 2017).
627 Modern conductivity of Lake Son Kol (515–530 $mS.cm^{-1}$) is about twice that of meromictic
628 Lake Bourget in France (300–350 $mS.cm^{-1}$). Therefore, mesopycnal (or homopycnal) flow
629 deposits occurred during periods of strong snowmelt (and/or increased temperatures),
630 indicated by the strong depletion of $\delta^{18}O$ in dark organic layers (Fig. 8), thus implying the
631 remobilization of sediments from the lake catchment whenever sufficient stream discharge
632 occurred to form a turbid plume. Two main factors control floods triggered by snowmelt: the
633 snowmelt potential and the actual melting. Snowmelt depends on the amount of seasonal solid
634 winter precipitation (e.g., snow) in the catchment while the intensity of melting is mostly
635 controlled by spring/summer temperature (Støren et al., 2010). During the warm Mid-
636 Holocene in Central Asia (Chen et al., 2008), periods of higher solid winter precipitation
637 coupled with relatively cool springs and warm summers may have favored increased
638 availability of snow when early summer temperatures started to rise in the mountains,
639 intensifying spring melt floods and the amount of terrestrial material washed into the lake.
640 Convective summer rainstorms during warm summers could also lead to lower lake water
641 $\delta^{18}O$ values during the Holocene thermal maximum. Intensive rainstorms in the summer
642 would increase hillslope erosion and stream discharge at a time when the lake was probably
643 more saline, stratified and shallow due to more intensive evaporation. Increased intensities of
644 rainstorms and snowmelt are therefore both possible drivers of mesopycnal or homopycnal
645 flows (and coarse sediment deposition) in Lake Son Kol. Alternatively, hypolimnetic anoxia
646 could have developed seasonally, by occurring under ice during the winter when organic
647 matter decomposes (if there is a limited snow cover that enables photosynthesis) and breaking
648 down towards the end of summer. However, this hypothesis is unlikely as (1) very few graded

649 beds related to ice melt are observed (i.e., resulting from the settling of fine-grained aeolian
650 particles deposited on ice to the lake bottom), (2) the regular occurrence of large phytoclasts
651 in dark organic layers with coarse minerogenic detritus (Fig. S6) implies a soil erosion from
652 the catchment, and thus is not compatible with aeolian depositional processes and, (3) Bphe *a*
653 data exhibit multi-annual periods of stratification (i.e., meromixis), rather than a seasonal
654 signal (Fig. 10).
655
656 *5.4. Holocene chemocline development*
657 The prominent changes in oxygenation conditions in the lake water column led to distinctive
658 changes in Lake Son Kol autotrophs (Figs. 9 and 10). Bphe *a* is produced by anoxygenic
659 phototrophic bacteria (APBs) which commonly live in the chemocline (oxic/anoxic transition)
660 of meromictic lakes (Overmann et al., 1991; Rogozin et al., 2012; Blankenship, 2013; Butz et
661 al., 2016). APBs require nutrients, sulphides and light to flourish, as provided by stable
662 chemocline (Parkin and Brock, 1980; Van Gemerden and Mas, 1995, Hodgson et al., 1998;
663 Madigan, 2003), and thus APBs may form dense populations in meromictic lakes (Van
664 Gemerden and Mas, 1995; McGowan et al, 2008). Such conditions usually develop when
665 lakes permanently stratify, but oxygen drawdown could also develop under ice with
666 respiration of organic matter, potentially leading to anoxic conditions during certain times of
667 the year when light is available and APB could flourish. Since dark organic-rich sediments
668 represent more than a single year in duration (Figs. 5 and 9), Bphe *a* suggest that the stability
669 of stratification increased and that there may have been periods of prolonged hypolimnetic
670 anoxia in Lake Kol during the Mid-Holocene. Recurring Bphe *a*, Br, S and ARO positive
671 anomalies (i.e., PC2 < 0) at 8500, 8400, 8200–7800, 7700–7500, 7300–7000, 6500–6100,
672 6000–5700 and 5500–5250 cal. yr BP thus imply periods characterized by the development of
673 a chemocline, which are tied to increased terrestrial inputs into the lake (PC1 > 0) (Fig. 9). A

very similar assemblage of spectral signatures (i.e., Bphe *a* and phycocyanin) was reported from Lake Qinghai (China), where higher Bphe *a* concentrations are tied to elevated freshwater inputs and increased warmth between ca. 8200 and 5500 cal. yr BP (Ji et al., 2009) (Fig. 10). This also coincides well with higher (alkenone-inferred) summer temperatures in Lake Balikun and Lake Qinghai at 8500–5000 cal. yr BP (Hou et al., 2016; Zhai et al., 2017). Warmer summers in Lake Jaczno (Poland) were also linked to the onset of lake meromixis (Butz et al., 2016). Besides, vegetation expansion in lake catchments during warm periods (and more specifically the expansion of broad-leaved trees, such as birch) is known to increase dissolved organic matter (DOM) fluxes to lakes and decrease UV light penetration (Sommaruga and Psenner, 1997; Schmidt et al., 2002). At Lake Son Kol, the presence of trees in the catchment and around the lake probably influenced lake trophic status and mixing conditions by (1) stimulating pedogenesis, which fueled oxygen consumption rates into the water body due to enhanced organic compounds exported to the lake and (2) sheltering the lake surface from wind-induced mixing (i.e., reduced wind exposure) thus favoring a prolonged time of stratification. Interestingly, the initiation of euxinic conditions in the hypolimnion (coeval to the deposition of dark organic-rich layers) followed the mass expansion of birch and arboreal taxa in the catchment between 8500 and 5000 cal. yr BP (Fig. 10), which enhanced terrestrial inputs of DOM and thus organic matter decomposition in the lake. Therefore pollen, geochemical and sedimentological proxies all suggest that hypolimnetic euxinia developed during warmer summers, and probably milder winters/springs. As proposed by Mathis et al. (2014), centennial-scale episodes of weakened seasonality indeed occurred between 8500 and 5000 cal. yr BP, alongside increased winter temperatures and warm summers hence promoting a longer growing season for the trees. Our findings also agree with other speleothem records from Central Asia which indicate increased moisture transport by the Westerlies, and higher winter/spring precipitation in the early part of

699 the Holocene (Fig. 10; Chen et al., 2016; Cai et al., 2017; Liu et al., 2019). In contrast, the
700 breakdown of lake stratification at 7500–7300 and 7000–6500 cal. yr BP probably coincides
701 with cooler climate conditions (and longer and thicker ice cover) linked to the strengthening
702 and southward position of the Siberian High in arid Central Asia. Increased influence of the
703 Siberian High would weaken the mid-latitude Westerlies and/or push their tracks further to
704 the south, resulting in comparably drier conditions in the Tian Shan (Aichner et al., 2015;
705 Wolff et al., 2017).
706
707 Enhanced nutrient concentrations (linked with higher soil development DOM supply to the
708 lake) are associated with a decrease in lake water transparency between 8500 and 7000 cal. yr
709 BP, judging from unstable values of oxygen phototrophs (Fig. 9). At roughly the same time,
710 phycocyanin abundances rapidly oscillate at high levels, suggesting that cyanobacteria
711 predominated over Chl *a* and derivatives. A similar pattern was reported from shallow lakes
712 in southern Sweden (Randsalu-Wendrup et al., 2014) and northern Germany (Dressler et al.,
713 2007). Therefore, cyanobacteria, which have the ability to sustain relatively high growth rates
714 at low light intensities (Mur et al., 1999), likely overtook oxygen phototrophs between 8500
715 and 7000 cal. yr BP, concurrently with the occurrence of APB blooms at the chemocline (Fig.
716 9). Before 5000 cal. yr BP, Lake Son Kol was a shallow and closed lacustrine system (Fig. 9;
717 Schwarz et al., 2017) and it is likely that a substantial proportion of the oxygen phototrophs
718 could derive from benthic algae (e.g., benthic diatoms and cyanobacteria). This also agrees
719 well with the occurrence of biofilms and/or microbial mat structures between 8500 and 5000
720 cal. yr BP (Pacton et al., 2015).
721
722 A major and abrupt change in lake regime is recorded around 5250 cal. yr BP in Lake Son
723 Kol, with a drastic decline of Bphe *a* concentrations that occurred within a decade or so (Figs.

724 9, 10). The abrupt decline in APB pigments indicates a rapid collapse of stratified conditions
725 and the breakdown of anoxic conditions in the hypolimnion after 5250 cal. yr BP, although
726 high Br and S are still recorded until ca. 5050 cal. yr BP. Because this event tipped the system
727 over a threshold (as observed in both PC1 and PC2 average model slopes; Figs. 6 and 7) into
728 another stable state from which former trophic and mixing conditions never recovered, we
729 consider this time interval as a tipping point in Lake Son Kol. A similar abrupt ecosystem
730 threshold was reported at 4900 cal. yr BP based on chironomid remains, and attributed to the
731 increased influence of the Westerlies causing enhanced precipitation and higher windiness at
732 Lake Son Kol (Schwarz et al., 2017; Laug et al., 2020). Drastic environmental change in the
733 lake may also be triggered by land-use processes in the catchment, which are mainly driven
734 by changes in grazing pressure at high altitudes. Abundance of coprophilous fungal
735 ascospores is assumed to reflect changes in grazing activity (Gauthier et al., 2010; Etienne et
736 al., 2013). Influxes of coprophilous fungi *sensu stricto* fluctuated between 0 and 10
737 spores.cm^{-2}.yr^{-1} between 6000 and 4000 cal. yr BP and during the last 2500 years (Fig. 10),
738 suggesting the predominance of wild animals in the Lake Son Kol catchment. Nevertheless
739 the presence of domestic herbivores cannot be excluded during 6000–4000 cal. yr BP, which
740 would match the occurrence of human fecal biomarkers in Lake Chatyr Kol sediments around
741 6000–5000 cal. yr BP (Schroeter et al., 2020). The imprint of domesticated livestock and
742 human occupation was likely highest around 3700 and 2500 cal. yr BP, where influxes
743 reached their maxima. Interestingly, influx values were generally stable during the period
744 5500–5000 cal. yr BP, when an abrupt ecosystem shift occurred in Lake Son Kol (Figs. 9,
745 10), thus implying that pastoralism apparently did not have a significant impact in the
746 catchment and that climate is the main driver of the abrupt regime shift identified around
747 5250 cal. yr BP.

748 After 5050 cal. yr BP, the lake became persistently well-mixed and the chemocline no longer
749 existed in the lake water column, as indicated by pervasive PC2 > 0 values (Fig. 9) and
750 elevated Mn content between 5000 and 3850 cal. yr BP that argue for oxic conditions in the
751 lake. Surprisingly, the advent of well-mixed conditions is closely related to a strong decline of
752 oxygen phototrophs (including cyanobacteria) between 5050 and 3850 cal. yr BP, with strong
753 negative anomalies around 4400–3800 cal. yr BP, coeval to high Mn anomalies (Fig. 9).
754 Because this phase corresponds to a noticeable decline in summer humidity and low lake
755 levels (PC1 < 0; Fig. 9), we posit that cooler summer temperatures and longer lasting and
756 thicker snow cover may have prevented the growth of oxygen phototrophs in the water
757 column (as well as the establishment of a stable stratification in summer after ice cover).
758 Alternatively, regular wind-driven lake mixing resulting from strengthened winds during the
759 spring ice break-up season (inducing stronger vertical water circulation) may have caused low
760 pigment deposition and preservation in the sediments (Cuddington and Leavitt, 1999). The
761 disappearance of the chemocline after 5050 cal. yr BP coincides with a decrease in terrestrial
762 DOM inputs into the lake, as catchment vegetation opened up with a decline of birch and
763 other arboreal taxa and a rise in *Artemisia* (Fig. 10; Mathis et al., 2014), similarly as in Lake
764 Qinghai (Ji et al., 2009). Tree removal around the lake thus probably led to higher wind
765 exposure of the open-water area (due to increased wind fetch), inducing in turn a better
766 mixing of the water column. Lake levels increased around 3700 cal. yr BP, corresponding to
767 another main tipping point based on high PC1 values (Fig. 6), in line with increased
768 planktonic diatom abundances and lower conductivities (Fig. 9; Schwarz et al., 2017). High
769 PC2 (and low Bphe *a*) values from 3800 cal. yr BP onwards infer that repetitive mixing
770 conditions prevented the establishment of a chemocline by oxygenating the hypolimnion
771 (Butz et al., 2016), which hampers the onset of stable temperature stratification during
772 summer. Such conditions promoted nutrient cycling in the photic zone to support oxygenic

phototrophs in the epilimnion, which diminished light penetration to the chemocline and led to the destruction of a suitable lake habitat for APB growth. Hence, all proxy data suggest that Lake Son Kol has had persistently high lake levels with well-mixed and oxygenated conditions for the last 5000 years, in accordance with its modern polymictic regime.

6. Conclusions and perspectives

Ultra-high temporal resolution geochemical and hyperspectral palaeolimnology data can yield a more complete understanding of changing ecological patterns and redox processes in shallow lacustrine systems. As a biomarker of planktonic APB at the chemocline of lakes, the presence/absence and variability of Bphe *a* in Lake Son Kol sediments provides crucial information about the timing and forcing mechanisms that control the advent and vanishing of lake stratification over the last thousands of years. Increased Bphe *a*, Br, S abundances along with higher terrestrial inputs from the catchment are recorded at 8500, 8400, 8200–7800, 7700–7500, 7300–7000, 6500–6100, 6000–5700 and 5500–5250 cal. yr BP, and involve recurring episodes of hypolimnetic anoxia and euxinic bottom water conditions coeval to the deposition of dark organic sediments on the lake floor. The presence of a chemocline and the associated deposition of coarse minerogenic detritus transported by concentrated flows appears to be dependent on recurrent seasonal snowmelt episodes, and thus on the quantity of snow and spring/summer temperatures that regulate the potential for meltwater events. Our data thus suggest that low lake levels and warmer climate conditions regularly prevailed during 8500–5250 cal. yr BP, and promoted massive APB blooms in a well-stratified lake system. After 5250 cal. yr BP, Son Kol water level recovered and the lake became persistently well mixed, leading to the disappearance of the chemocline. This abrupt ecosystem shift was associated with cooler conditions and strengthened wind forcing, when the influence of the Westerlies increased from 5250 cal. yr BP onwards. Intensified wind forcing also most

probably coincided with a significant increase of wave activity at the lake shoreline acting as an erosive agent. The imprint of wind forcing on coastal sedimentary dynamics (e.g., littoral sand drift) and geomorphological processes can be observed based on the diagnostic sedimentary features along the northeastern and southeastern shores of the lake, where sand spits, wave-dominated beaches, barrier spits and associated open lagoons have developed, hence suggesting that Lake Son Kol is presently a wind-driven water body (as defined by Nutz et al., 2018). Further studies are required in order to properly date such geomorphological features and assess the relationships between wind forcing, past lake levels and climatic trends during the Mid- to Late Holocene.

Acknowledgments

We are grateful to Anne-Lise Develle (EDYTEM) for conducting XRF core-scanner analyses on core SK06. The hyperspectral imaging acquisition was conducted at the University of Normandie-Rouen. This research was funded by the Laboratory of Geology of Lyon (LGL-TPE). All data from Son Kol core SK06 are available as supplementary data via the QSR network.

Figure captions:

Figure 1: Location of Lake Son Kol: (a) global map with focus on western central Asia; (b) central Tian Shan including south Kazakhstan and Lake Balkash (image courtesy of NASA GSFC); and (c) bathymetric map of the lake, with isobaths given in meters below lake level (modified after Academy of Science of the Kyrgyz SSR, 1987). Orange points refer to sediment core SK06, while the two yellow and the white points indicate cores SK07 and SK04 (Mathis et al., 2014; Huang et al., 2014; Pacton et al., 2015) and SONK_11_D1/2

(Lauterbach et al., 2014), respectively.

Figure 2: (a) Detailed stratigraphic correlation between cores SK06 (this study) and cores SK04 and SK07 (Huang et al., 2014; Mathis et al., 2014) from Lake Son Kol using distinct lithological marker layers. Studied cores are located on the map provided in Fig. 1. (b) Age model for core SK06 based on the *P_Sequence* depositional model (model parameter k=1) established using Oxcal 4.4 (Ramsey, 1995, 1998, 2001). The blue envelope corresponds to the 2σ probability range. See text for detail.

Figure 3: (a) Visible signatures and (b) continuum removal spectra with associated main absorptions for Chl *a* (and derivatives), phycocyanin and Bphe *a* (Bacteriopheophytin *a*) from three selected intervals in which these pigments are abundant in core SK06.

Figure 4: (a) PCA biplot of major elements obtained by XRF core scanner and hyperspectral analyses (PC1 vs PC2). PC1 vs PC3 and PC2 vs PC3 are shown in Fig. S4. (b) Comparison between Ca, Fe and Ti content from XRF core-scanner and discrete XRF analyses in core SK07.

Figure 5: Hyperspectral image and spectral indices (relative absorption band area or RABA) for core SK06. From left to right: 500-µm resolution Br and S (XRF core-scanner), distribution maps and plots of Chl *a* plus derivatives (RABA630–700), phycocyanin (RABA600–630), Bacteriopheophytin (Bphe *a*) (RABA750–900) and aromatic organic matter (ARO; RABA1660–1690), respectively. Grey shadings outline intervals with higher Br, S, phycocyanin and Bphe *a* contents, which are tied to the occurrence of dark organic

sediments in core SK06. Yellow shadings outline intervals with elevated content in Chl *a* and phycocyanin in core SK06.

Figure 6: Average changepoint model's slope calculated for PC1. The green curve in the individual plots outlines the most pronounced regime shift identified around 5050 cal. yr BP. Purple-filled curves correspond to abrupt shifts identified in both PC1 and PC2.

Figure 7: Average changepoint model's slope calculated for PC2. The green curve in the individual plots outlines the most pronounced regime shift identified around 5250 cal. yr BP. Purple-filled curves correspond to abrupt shifts identified in both PC1 and PC2.

Figure 8: Close-up on XRF and hyperspectral data for the interval 131.5–151.5 cm in core SK06 (ca. 6500–5600 cal. yr BP), plotted against grain size (clay, sand), stable isotope ($\delta^{18}O$, $\delta^{13}C_{org}$), total organic matter (TOC), total carbon (TC), total nitrogen (TN) and C/N data from core SK07 in Lake Son Kol (Huang et al. 2014; unpublished data). Yellow shadings refer to intervals characterized by dark organic layers with coarser minerogenic detritus, high Br, S, Bphe *a*, ARO in core SK06, as well as high TOC (and TC, TN and C/N) and depleted $\delta^{18}O$ and $\delta^{13}C_{org}$ values in core SK07.

Figure 9: Time series of hyperspectral, geochemical and PCA data for Lake Son Kol (core SK06), plotted with proxy data from core SONK_11_D1/2 from Lake Son Kol (Lauterbach et al., 2014; Schwarz et al., 2017). XRF (9-point running means) and hyperspectral data (15-point running means) for core SK06 are represented as standardized values (mean = 0, standard deviation = 1). Yellow shadings outline periods for which hypolimnetic euxinia prevailed in Lake Son Kol. See text for detail.

872

873 **Figure 10:** Comparison of geochemical and palynological proxies from Lake Son Kol to
874 other regional records in Central Asia. Shaded areas indicate periods characterized by
875 relatively warm summers and milder winters/springs with intensified precipitation (rain or
876 snow) at Lake Son Kol, favoring enhanced winter/spring snow thaw episodes; (a) Bphe *a*
877 record from Lake Qinghai, China (Ji et al., 2009); (b) alkenone-inferred temperature record at
878 Lake Qinghai (Hou et al., 2016); (c) speleothem $\delta^{18}O$ record from Tonnel'naya (Ton) Cave,
879 Uzbekistan (Chen et al., 2016); (d) speleothem $\delta^{18}O$ record from Baluk Cave, China (Liu et
880 al., 2019); (e) influx of coprophilous fungi *sensu stricto* (core SK06, this study); (f) arboreal
881 pollen (%) record from Lake Son Kol, Kyrgyzstan (Mathis et al., 2014); (g) total content of
882 Betulaceae (%) from Lake Son Kol, Kyrgyzstan (Mathis et al., 2014) and (h) Bphe *a* record
883 (15-point running means) from Lake Son Kol (core SK06, this study).

884

885 **Figure S1:** Core-to-core correlation between sediment cores SK06, SK04 and SK06 using
886 magnetic susceptibility.

887

888 **Figure S2:** Correlation of core SK06 (this study) with core SONK_11_D1/2 from Lauterbach
889 et al., (2014) using distinct lithological marker layers.

890

891 **Figure S3:** 500-µm resolution (grey curves) XRF core-scanner data exhibiting Br, S, Ti, Rb,
892 Zr, Fe, Si, Ca, Sr and Mn. Red curves represent 31-point running means. Yellow shadings
893 outline intervals with high Br, S, Ti, Rb and low Zr, Ca, Sr and Mn, which are tied to the
894 occurrence of dark organic sediments in core SK06.

895

Figure S4: PCA biplots of major elements obtained by XRF core scanner and hyperspectral analyses (PC1 vs PC3 and PC2 vs PC3).

Figure S5: Average changepoint models of PC1 and PC2 during the last 8500 years in core SK06.

Figure S6: Thin-section images (cross-polarized light) of the detrital layer microfacies types observed in dark organic-rich sediments; (a) minerogenic detrital layer characterized by rare normal graded beds in a non-graded matrix-supported (i.e., fine silt) layer. Note the absence of a sharp erosive basal layer; (b) a typical detrital layer exhibiting mixed organic (e.g., phytoclasts), bioclasts (e.g., ostracod valves) and minerogenic detritus. Note the absence of grading into the detrital layer; (c, d) organic detrital layer mainly consisting of phytoclasts, interpreted as reworked terrestrial material (sheet-wash) from the catchment.

Table 1: AMS ^{14}C dates obtained on terrestrial plan remains and bulk sediment OM (with unknown proportion of aquatic OM) in cores SK07 and SK04 (Huang et al., 2014) and core SONK_11_D1/2 (Lauterbach et al., 2014). Published AMS ^{14}C dates were transposed to core SK06 using lithological and magnetic susceptibility-inferred correlations (Figs. 2a, S1 and S2). Conventional ^{14}C ages were calibrated using Oxcal 4.4 with the IntCal20 calibration dataset (Reimer et al., 2020). A reservoir correction of 150 years was applied before calibration to conventional ^{14}C ages. Only the samples with asterisks (*) were considered for age modeling (see text for detail).

References

921 Abramowski U, Bergau A, Seebach D et al. (2006) Pleistocene glaciations of Central Asia:
922 results from ^{10}Be surface exposure ages of erratic boulders from the Pamir (Tajikistan) and
923 the Alay-Turkestan range (Kyrgyzstan). Quat Sci Rev 25:1080–1096
924
925 Academy of Science of the Kyryz SSR (1987) Atlas of the Kyrgyz Soviet Socialist Republic.
926 Volume 1: Natural conditions and resources. Moscow: State Agency for Cartography and
927 Geodesy, Central Directorate for Geodesy and Cartography, Council of Ministers of the
928 USSR
929
930 Adrian R, Deneke R, Mischke U et al. (1995) A long-term study of the Heiligensee (1975–
931 1992). Evidence for effects of climatic change on the dynamics of eutrophied lake
932 ecosystems. Arch Hydrobiol 133(3):315–337
933
934 Aichner B, Feakins SJ, Lee JE et al. (2015) High-resolution leaf wax carbon and hydrogen
935 isotopic record of the late Holocene paleoclimate in arid Central Asia. Clim Past 11:619–633
936
937 Aizen VB, Aizen EM, Melack JM et al. (1997) Climatic and hydrologic changes in the Tien
938 Shan, Central Asia. Journal of Climate 10:1393–1404
939
940 Alley RB, Mayewski PA, Sowers T et al. (1997) Holocene climate instability: a large event
941 8000–8400 years ago. Geology 25:482–486
942
943 Appleby PG, Richardson N, Nolan PJ (1991) ^{241}Am dating of lake sediments. Hydrobiologia
944 214:35–42
945

946 Balsam WL, Damuth JE, Schneider RR (1997) Comparison of shipboard vs. shorebased
947 spectral data from Amazon Fan cores: implications for interpreting sediment composition.
948 Ocean Drill Prog Sci 155:193–215
949
950 Balsam WL, Deaton BC (1996) Determining the composition of Late Quaternary marine
951 sediments from NUV, VIS, and NIR diffuse reflectance spectra. Marine Geol 134:31–55
952
953 Barranco FT, Balsam WL, Deaton BC (1989) Quantitative reassessment of brick red lutites—
954 evidence from reflectance spectrophotometry. Marine Geol 89:299–314
955
956 Bates CC (1953) Rational theory of delta formation: AAPG Bulletin 37(9):2119–2162
957
958 Beer R, Heiri O, Tinner W (2007) Vegetation history, fire history and lake development
959 recorded for 6300 years by pollen, charcoal, loss on ignition and chironomids at a small lake
960 in southern Kyrgyzstan (Alay Range, Central Asia). The Holocene 17:977–985
961
962 Beloglasova VN, Smirnova NB (1987). Atlas Kirgizskoj SSR. GUGK SSSR, Bishkek (in
963 Russian)
964
965 Blankenship RE (2013) Molecular mechanisms of photosynthesis. John Wiley& Sons.
966
967 Bugaev VA, Dzhordzhio VA, Kozik EM et al. (1957) Sinopticheskie Protsessy Sredney Azii
968 (Synoptic processes in Central Asia). Izd Akad Nauk Uzbek, SSR, Tashkent, 447 pp
969
970 Butz C, Grosjean M, Poraj-Górska A et al. (2016) Bacteriopheophytin *a* as an indicator of

meromixis in sediments of Lake Jaczno, north-east Poland, CE 1891–2010. Glob Planet Change 144:109–118

Butz C, Grosjean M, Fischer D et al. (2015) Hyperspectral imaging spectroscopy: a promising method for the biogeochemical analysis of lake sediments. J Appl Remote Sens 9:1–20

Cai Y, Chiang JCH, Breitenbach SFM et al. (2017) Holocene moisture changes in western China, Central Asia, inferred from stalagmites. Quat Sci Rev 158:15–28

Chapron E, Arnaud F, Noel H et al. (2005) Rhône River flood deposits in Lake Le Bourget: a proxy for Holocene environmental changes in the NW Alps, France. Boreas 31:1–13

Chapron E, Van Rensbergen P, De Batist M et al. (2004) Fluid-escape features as a precursor of a large sublacustrine sediment slide in Lake Le Bourget, NWAlps, France. Terra Nova 16:305–311

Chen Y, Li W, Deng H et al. (2016) Changes in Central Asia's water tower: Past, present and future. Scientific Reports 6, https://doi.org/10.1038/srep35458

Chen FH, Chen JH, Holmes JA et al. (2010) Moisture changes over the last millennium in the arid central Asia: A review, synthesis and comparison with monsoon region. Quat Sci Rev 29:1055–1068

Chen FH, Yu ZC, Yang ML et al. (2008) Holocene moisture evolution in arid central Asia and its out-of-phase relationship with Asian monsoon history. Quat Sci Rev 27:351–364

996

997 Christensen JH et al (2017) Regional Climate Projections. Climate Change 2007: the Physical
998 basis, 847–940

999

1000 Coolen MJL, Overmann J (1998) Analysis of subfossil molecular remains of purle sulphur
1001 bacteria in a lake sediment. App Env Microbiol 64(11):4513–4521

1002

1003 Cuddington K, Leavitt PR (1999) An individual-based mode of pigment flux in lakes:
1004 implications for organic biogeochemistry and paleoecology. Can J Fish Aqua Sci 56(10):
1005 1964–1977

1006

1007 Cugny C, Mazier F, Galop D (2010) Modern and fossil non-pollen palynomorphs from the
1008 Basque mountains (western Pyrenees, France): the use of coprophilous fungi to reconstruct
1009 pastoral activity. Veget Hist Archaebot 19:391–408

1010

1011 Cuven S, Francus P, Lamoureux SF (2010) Estimation of grain size variability with micro X-
1012 ray fluorescence in laminated lacustrine sediments, Cape Bounty, Canadian High Arctic. J
1013 Paleolimnol: doi10.1007/s10933-010-9453-1

1014

1015 Das B, Vinebrooke RD, Sanchez-Azofeifa A et al. (2005) Inferring lake sediment chlorophyll
1016 concentrations with reflectance spectroscopy: a novel approach to
1017 reconstructing trophic status changes in alpine lakes. Can J Fish Aquat Sci 62:1067–1078

1018

1019 Davies SJ, Lamb HF, Roberts S (2015) Micro-XRF core scanning in palaeolimnology: recent
1020 developments. In: Croudace I, Rothwell R (eds) Micro-XRF Studies of Sediment Cores.
1021 Developments in Paleoenvironmental Research, vol 17. Springer, Dordrecht
1022
1023 Davies OK, Schafer D (2006) *Sporormiella* fungal spores, a palynological means of detecting
1024 herbivore density. Palaeogeo, Palaeoclimato., Palaeoecol. 237:40–50
1025
1026 Davison W (1993) Iron and Manganese in lakes. Earth Sci Rev 34(2):119–163
1027
1028 Dressler M, Hübener T, Görs S et al. (2007) Multi-proxy reconstruction of trophic state,
1029 hypolimnetic anoxia and phototrophic sulphur bacteria abundance in a dimictic lake in
1030 Northern Germany over the past 80 years. J Paleolimnol 37:205–219
1031
1032 Etienne D, Wilhelm B, Sabatier P et al. (2013) Influence of sample location and livestock
1033 numbers on *Sporormiella* concentrations and accumulation rates in surface sediments of Lake
1034 Allos, French Alps. J Paleolimnol 49:117–127
1035
1036 Faegri K, Iversen J (1989) Textbook of pollen analysus. John Wiley and Sons, Chichester-
1037 New York-Brisbane-Toronto-Singapore.
1038
1039 Feeser I, O'Connell M (2009) Fresh insights into long-term changes in flora, vegetation, land
1040 use and soil erosion in the karstic environment of the Burren, western Ireland. Journal of
1041 Ecology 97(5):1083–1100
1042
1043 Foley B, Jones ID, Maberly SC et al. (2012) Long term changes in oxygen depletion in a

1044 small temperate lake: effects of climate change and eutrophication. Freshw Biol 57(2):278–
1045 289
1046
1047 Gallagher K, Bodin T, Sambridge M, Weiss D, Kylander M, Large D (2011) Inference of
1048 abrupt changes in noisy geochemical records using transdimensional change point models.
1049 Earth and Planetary Science Letters 311 :182–194
1050
1051 Gauthier E, Bichet V, Massa C, Petit C et al. (2010) Pollen and non-pollen palynomoprh
1052 evidence of medieval farming activities in southwestern Greenland. Veget Hist Archaeobot
1053 19:427–438
1054
1055 Gelorini V, Verbeken A, van Geel B et al. (2011) Modern non-pollen palynomorphs from
1056 East African lake sediments. Rev Palaeobot Palynol 164(3–4):143–173
1057
1058 Giguet-Covex C, Arnaud F, Poulenard J et al. (2011) Changes in erosion patterns during the
1059 Holocene in a currently treeless subalpine catchment inferred from lake sediment
1060 geochemistry (Lake Anterne, 2063 m.a.s.l, NW France): the role of climate and human
1061 activities. The Holocene 21:651–665
1062
1063 Glazer AN, Fang S, Brown DM (1973) Spectroscopic properties of C-Phycocyanin and of its
1064 α and β subunits. The Journal of Biological Chemistry 248(16):5679–5685
1065
1066 Håkanson L, Jansoon M (1983) Principles of lake sedimentology. Heidelberg, Springer
1067 Verlag, 312 pp
1068

1069 Hammer Ø, Harper DAT, Ryan PD (2001) PAST: Paleontological Statistics Software
1070 Package for Education and Data Analysis. Palaeontologia Electronica 4(1), 9p.
1071
1072 Heinecke L, Fletcher WJ, Mischke S et al. (2018) Vegetation change in the eastern Pamir
1073 Mountains, Tajikistan, inferred from Lake Karakul pollen spectra of the last 28 kyr.
1074 Palaeogeogr Palaeoclimatol Palaeocol 511(15):232–242
1075
1076 Heinecke L, Mischke S, Adler K et al. (2017) Climatic and limnological changes at Lake
1077 Karakul (Tajikistan) during the last ~29 cal ka. J Paleolimnol 58:317–334
1078
1079 Heinecke L, Mischke S, Adler K et al. (2016) Late Pleistocene to Holocene climate and
1080 limnological changes ar Lake Karakul (Pamir Mountains, Tajikistan). Clim Past Discuss,
1081 doi:10.5194/cp-2016-34
1082
1083 Heymann C, Nelle O, Dörfler W et al. (2013) Late Glacial to Mid-Holocene palaeoclimates
1084 development of Southern Greece inferred from the sediment sequence of Lake Stymphalia
1085 (NE Peloponnese). Quat Int 302:42–60
1086
1087 Hodgson D, Wright S, Tyler P et al. (1998) Analysis of fossil pigments from algae and
1088 bacteria in meromictic Lake Fidler, Tasmania, and its application to lake management. J
1089 Paleolimnol 19(1):1–22
1090
1091 Horváth H, Kovacs AW, Riddick C et al. (2013) Extraction methods for phycocyanin
1092 determination in freshwater filamentous cyanobacteria and their application in a shallow lake.
1093 Eur J Phycol 48(3):278–286

1094

1095 Hou J, Huang Y, Zhao J et al. (2016) Large Holocene summer temperature oscillations and
1096 impact on the peopling of the northeastern Tibetan Plateau. Geophys res Lett 43 :1323–1330

1097

1098 Huang X, Oberhänsli H, von Suchodoletz H et al. (2014) Hydrological changes in western
1099 Central Asia (Kyrgyzstan) during the Holocene: Results of a paleolimnological study from
1100 Son Kul. Quat Sci Rev 103:134–152

1101

1102 IPCC (2013) Climate Change 2013: The Physical Science Basis. Contribution of Working
1103 Group I to the Fifth Assessment Report of the Intergovernmental Panel on Climate Change.
1104 Cambridge; New York: Cambridge University Press, 1535 pp

1105

1106 Jacq K, Martinez-Lamas R, Van Exem A, Debret M (2020) Hyperspectral core-logger image
1107 acquisition. Protocols io, https://protocols.io/view/hyperspectral-core-logger-image-
1108 acquisition-bikckcsw

1109

1110 Jenny JP, Arnaud F, Dorioz JM et al. (2013) A spatiotemporal investigation of varved
1111 sediments highlights the dynamics of hypolimnetic hypoxia in a large hard-water lake over
1112 the last 150 years. Limnol Oceanogr 58(4):1395–1408

1113

1114 Ji J, Balsam W, Shen J et al. (2009) Centennial blooming of anoxygenic phototrophic bacteria
1115 in Qinghai Lake linked to solar and monsoon activities during the last 18,000 years. Quat Sci
1116 Rev 28:1304–1308

1117

1118 Kalff J (2002) Limnology: Inland Water Ecosystems. Prentice Hall, 592 pp

1119

1120 Koppes M, Gillespie AR, Burke RM et al. (2008) Late Quaternary glaciation in the Kyrgyz

1121 Tien Shan. Quat Sci Rev 27:846–866

1122

1123 Laug A, Schwarz A, Lauterbach S et al. (2020) Ecosystem shifts at two Mid-Holocene tipping

1124 points in the alpine Lake Son Kol (Kyrgyzstan, Central Asia). The Holocene,

1125 doi:10.1177/0959683620932973

1126

1127 Lauterbach S, Witt R, Plessen B et al. (2014) Climatic imprint of the mid-latitude Westerlies

1128 in the Central Tien Shan of Kyrgyzstan and teleconnections to North Atlantic climate

1129 variability during the last 6000 years. The Holocene 24(8):970–984

1130

1131 Lenton TM (2011) Early warming of climate tipping points. Nat Clim Change 1:201–209

1132

1133 Lenton TM, Held H, Kriegler E et al. (2008) Tipping elements in the Earth"s climate system.

1134 Proc Nat Acad Sci USA 105:1786–1793

1135

1136 Li X, Zhao K, Dodson J et al. (2011) Moisture dynamics in central Asia for the last 15 kyr:

1137 New evidence from Yili Valley, Xinjiang, NW China. Quat Sci Rev 30:3457–3466

1138

1139 Liu, X, Rao, Z, Shen CC et al. (2019) Holocene solar activity imprint on centennial- to

1140 multidecadal-scale hydroclimatic oscillations in Arid Central Asia. JGR Atmospheres

1141 124:2562–2573

1142

1143 Livingstone DM (2003) Impact of secular ckimate change on the thermal structure of a large

1144 temperate central European lake. Clim Change 57(1–2):205–225
1145
1146 Machalett B, Oches EA, Frechen M et al. (2008) Aeolian dust dynamics in Central Asia
1147 during the Pleistocene: driven by the long-term migration, seasonality and permanency of the
1148 Asiatic polar front. Geochemistry, Geophysics, Geosystems 9:Q08Q09
1149
1150 Machalett B, Frechen B, Hambach U et al (2006) The loess sequence from Remisowka
1151 (northern boundary of the Tien Shan Mountains (Kazakhstan). Part I: luminescence dating.
1152 Quat Int 152–153:192–201
1153
1154 Madigan MT (2003) Anoxygenic phototrophic bacteria from extreme environments.
1155 Photosynth Res 76:157–171
1156
1157 Mathis M, Sorrel P, Klotz S et al. (2014) Regional vegetation patterns at lake Son Kul reveal
1158 Holocene climatic variability in central Tien Shan (Kyrgyzstan, Central Asia). Quat Sci Rev
1159 89:169–185
1160
1161 McGowan S, Juhler RK, Anderson NJ (2008) Autotrophic response to lake age, conductivity
1162 and temperature in two West Greenland lakes. J Paleolimnol 39:301–317
1163
1164 Michelutti N, Blais JM, Cumming BF et al. (2010) Do spectrally inferred determinations of
1165 chlorophyll *a* reflect trends in lake trophic status? J Paleolimnol 43:205–217
1166
1167 Mischke S, Rajabov I, Mustaeva N et al. (2010) Modern hydrology and late Holocene history
1168 of Lake Karakul, eastern Pamirs (Tajikistan): A reconnaissance study. Palaeogeogr

1169 Palaeoclimatol Palaeocol 289:10–24
1170
1171 Mulder T, Chapron E (2011) Flood deposits in continental and marine environments:
1172 Character and significance, in R. M. Slatt and C. Zavala (eds) Sediment transfer from shelf to
1173 deep water–Revisiting the delivery system: AAPG Studies in Geology 61:1–30
1174
1175 Mur LR, Skulberg OM, Utkilen H (1999) Cyanobacteria in the environment. In: Chorus I,
1176 Bartram J (eds) Toxic cyanobacteria in water: a guide to their public health consequences,
1177 monitoring and management. E & FN Spon, London
1178
1179 Narama C, Kondo R, Tsukamoto S et al. (2007) OSL dating of glacial deposits during the last
1180 glacial in the Terskey-Alatoo range, Kyrgyz Republic. Quat Geochronol 2:249–254
1181
1182 Narama C, Okuno M (2006) Record of a glacier variations during the last glacial in the
1183 Turkestan Range of Pamir-Alay, Kyrgyz Republic. Ann Glaciol 43:397–404
1184
1185 Oren A (2011) Characterization of pigments of prokaryotes and their use in taxonomy and
1186 classification. In : Methods in Microbiology, Academic Press, pp. 261–282.
1187
1188 Overmann J, Beatty JT, Hall KJ et al. (1991) Characterization of a dense, purple sulfur
1189 bacteria layer in a meromictic salt lake. Limnol Oceanogr 36(5):846–859
1190
1191 Ozturk T, Altinsoy H, Türkes M et al. (2012) Simulation of temperature and precipitation
1192 climatology for the Central Asia CORDEX domain using RegCM 4.0. Climate Research
1193 52:63–76

1194

1195 Pacton M, Sorrel P, Bevillard B et al. (2015) Sedimentary facies analyses from nano- to
1196 millemetre scale exploring past microbial activity in a high-altitude lake (Lake Son Kul,
1197 Central Asia). Geol Mag 152(5):902–922

1198

1199 Parkin T, Brock T (1980) Photosynthetic bacterial production in lakes: the effects of light
1200 intensity. Limnol Oceanogr 25(4):711–718

1201

1202 Ramsey CB (2008) Deposition models for chronological records. Quat Sci Rev 27:42–60

1203

1204 Ramsey CB (2001) Development of the radiocarbon calibration program. Radiocarbon
1205 43:355–363

1206

1207 Ramsey CB (1995) Radiocarbon calibration and analysis of stratigraphy: The OxCal program.
1208 Radiocarbon 37:425–430

1209

1210 Randsalu-Wendrup L, Conley D, Carstensen J et al. (2014) Combining limnology and
1211 palaeolimnology to investigate recent regime shifts in a shallow, eutrophic lake. J Paleolimnol
1212 51:437–448

1213

1214 Reimer PJ, Austin EN, Bard E et al. (2020) The IntCal20 Northern Hemisphere radiocarbon
1215 age calibration curve (0–55 cal kBP). Radiocarbon 62(4):725–757

1216

1217 Rein B, Sirocko F (2002) In-situ reflectance spectroscopy— analysing techniques for high-
1218 resolution pigment logging in sediment cores. Int J Earth Sci 91:950–954

1219

1220 Rogozin DY, Zykov VV, Degetmendzhi AG (2012) Ecology of purple sulfur bacteria in the
1221 highly stratified meromictic Lake Shunet (Siberia, Khakassia) in 2002–2009. Microbiology
1222 81(6) :727–735

1223

1224 Rohling EJ, Pälike H (2005) Centennial-scale climate cooling with a sudden cold event
1225 around 8,200 years ago. Nature 434:975–979

1226

1227 Rousseau M, Demory F, Miramont C et al. (2020) Palaeoenvironmental change and glacier
1228 fluctuations in the high Tien Shan Mountains during the last millennium based on sediments
1229 from Lake Ala Kol, Kyrgyzstan. Pal Pal Pal 558, 109987.

1230

1231 Savoskul OS, Solomina ON (1996) Late Holocene glacier variations in the frontal and inner
1232 ranges of the Tien Shan, central Asia. The Holocene 6(1):25–35

1233

1234 Scheer H (2006) An overview of chlorophylls and bacteriochlorophylls : biochemistry,
1235 biophysics, functions and applications. In : Grimm B, Porra R, Rüdiger W, Scheer H (Eds),
1236 Chlorophylls and bacteriochlorophylls Advances in Photosynthesis and Respiration. Springer,
1237 Netherlands:1–26

1238

1239 Scheffer M, Carpenter SR, Lenton TM et al. (2012) Anticipating critical transitions. Science
1240 338:344–348

1241

1242 Schmidt R, Psenner R, Müller J et al. (2002) Impact of late glacial climate variations on
1243 stratification and trophic state of the meromictic lake Längsee (Austria): validation of a

conceptual model by multi-proxy studies. J Limnol 61(1):49–60

Schröder HG, Wessels M, Niessen F (1998) Acoustic facies and depositional structures of Lake Constance. Archiv fur Hydrobiologie Special Issues Advance Limnology 53:351–368

Schroeter N, Lauterbach S, Stebich M et al. (2020) Biomolecular evidence of early human occupation of a high-altitude site in Western Central Asia during the Holocene. Front Earth Sci 8, doi:10.3389/feart.2020.00020

Schwarz A, Turner F, Lauterbach S et al. (2017) Mid- to Late Holocene climate-driven regime shifts inferred from diatom, ostracod and stable isotope records from Lake Son Kol (Central Tien Shan, Kyrgyzstan). Quat Sci Rev 177:340–356

Shnitnikov AV (1980) Ozera Tian-Shanya i ikh istoriya [Lakes of the Tian Shan and their history]. Leningrad: Nauka.

Solomon S, Qin D, Manning M et al. (eds) 2007 Climate Change 2007: The Physical Science Basis (Contribution of Working Group I to the Fourth Assessment Report of the Intergovernmental Panel on Climate Change). Cambridge: Cambridge University Press

Sommaruga R, Psenner R (1997) Ultraviolet radiation in a high mountain lake of the Austrian Alps: Air and underwater measurements. Photochemistry and Photobiology 65:957–963

Stockmarr J (1971) Tablets with spores used in absolute pollen analysis. Pollen spores 13:615–621

1269

1270 Støren EN, Dahl SO, Nesje A et al. (2010) Identifying the sedimentary imprint of high-
1271 frequency Holocene river floods in lake sediments: development and application of a new
1272 method. Quat Sci Rev 29:3021–3033

1273

1274 Trachsel M, Grosjean M, Schnyder D et al. (2010) Scanning reflectance spectroscopy (380–
1275 730 nm): a novel method for quantitative high-resolution climate reconstructions from
1276 minerogenic lake sediments. J Paleolimnol 44:979–994

1277

1278 van Geel B, Andersen ST (1988) Fossil ascospores of the parasitic fungus Ustulina deusta in
1279 Eemian deposits in Denmark. Rev Palaeobot Palynol 56:89–93

1280

1281 van Geel B, Aptroot A (2006) Fossil ascomycetes in Quaternary deposits. Nova Hedwigia
1282 82:313–329

1283

1284 van Geel B, Buuman J, Brinkkemper O et al. (2003) Environmental reconstruction of a
1285 Roman Period settlement site in Uitgeest (The Netherlands), with special reference to
1286 coprophilous fungi. J Archaeol Sci 30:873–883

1287

1288 Van Gemerden H, Mas J (1995) Ecology of phototrophic bacteria. In : Blankenship R,
1289 Madigan M, Bauer C (Eds) Anoxygenic photosynthetic bacteria. Advances in photosynthesis
1290 and respiration. Springer, Netherlands : pp 49–85

1291

1292 Van Rensbergen P, De Batist M, Beck C et al. (1999) High-resolution seismic stratigraphy of
1293 glacial to interglacial fill of a deep glacigenic lake: Lake Le Bourget, Northwestern Alps,

France. Sed Geol 128:99–129

Van Rensbergen P, De Batist M, Beck C et al. (1998) High-resolution seismic stratigraphy of late Quaternary fill of Lake Annecy (Northwestern Alps): evolution from glacial to interglacial sedimentary processes. Sed Geol 117:71–96

Wheeler OH (1959) Near infrared spectra of organic coumpounds. Chem Rev 59:629–666

Williams RC, Gingrich JC, Glazer AN (1980) Cyanobacterial phycobilisomes. J Cell Biol 85:558–566

Wirth S, Gili A, Niemann H et al. (2013) Combining sedimentological, trace metal (Mn, Mo) and molecular evidence for reconstructing past water-column redox conditions: The example of meromictic Lake Cadagno (Swiss Alps). Geoch Cosmoch Acta 120:220–238

Wolfe AP, Vinebrooke RD, Michelutti N et al. (2006) Experimental calibration of lake-sediment spectral reflectance to Chlorophyll a concentrations: methodology and paleolimnological validation. J Paleolimnol 36:91–100

Wolff C, Plessen B, Dudashvilli AS et al. (2017) Precipitation evolution of Central Asia during the last 5000 years. The Holocene, DOI: 10.1177/0959683616652711

Woźniak M, Bradtke K, Darecki M et al. (2016) Empirical model for phycocyanin concentration estimation as an indicator of cyanobacterial bloom in the optically complex coastal waters of the Baltic Sea. Remote Sens 8(3): 212, https://doi.org/10.3390/rs8030212

Yacobi YZ, Köhler J, Leunert F et al. (2015) Phycocyanin-specific absorption coefficient: eliminating the effect of chlorophyll absorption. Limnol and Oceanogr Methods 13(4):157–1168

Zhao J, An C-B, Huang Y et al. (2017) Contrasting early Holocene temperature variations between monsoonal East Asia and westerly dominated Central Asia. Quat Sci Rev 178:14–23

Zyakun AM, Lunina ON, Prusakov TS et al. (2009) Fractionation of stable carbon isotopes by photoautrophically growing anoxygenic purple and green sulfur bacteria. Microbiology 78(6):757–768

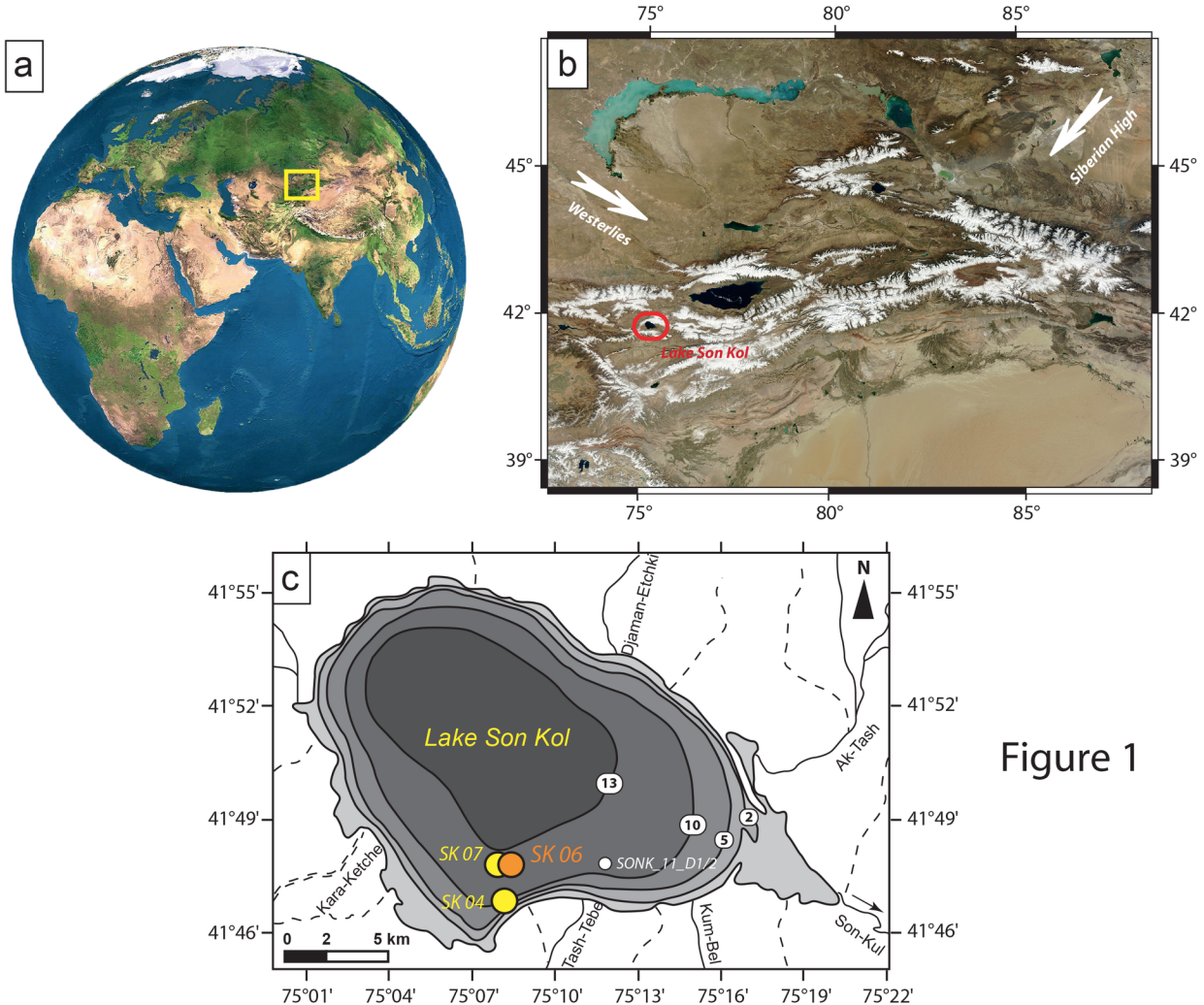
a
b
75°
80°
85°
45°
42°
39°
Westerlies
Siberian High
Lake Son Kol
c
41°55'
41°52'
41°49'
41°46'
N
Djaman-Etchki
Ak-Tash
Lake Son Kol
13
10
5
2
SK 07
SK 06
SK 04
SONK_11_D1/2
Kara-Ketche
Tash-Tebe
Kum-Bel
Son-Kul
0 2 5 km
75°01'
75°04'
75°07'
75°10'
75°13'
75°16'
75°19'
75°22'

Figure 1

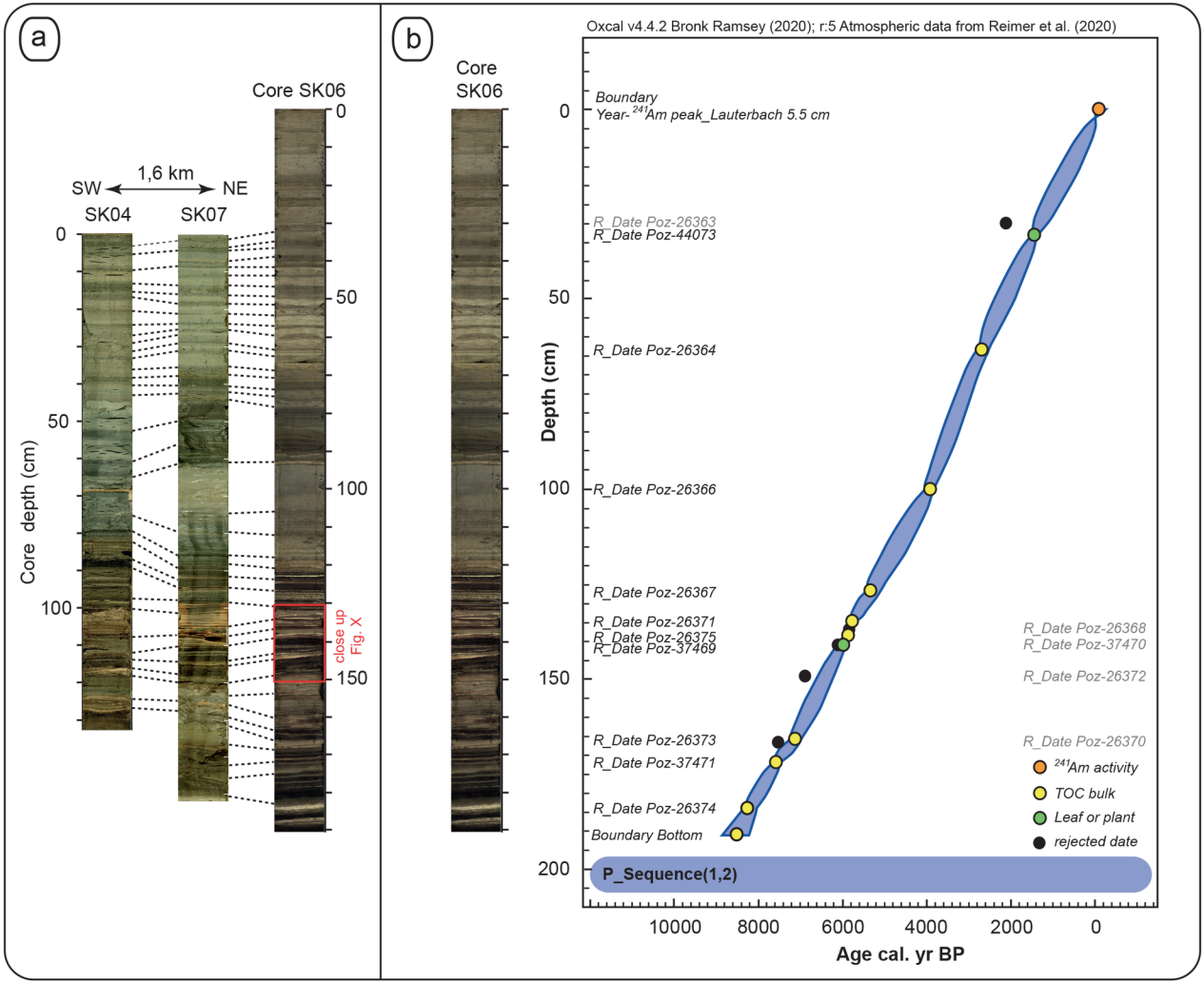
a
Core SK06
0
1,6 km
SW
NE
SK04
SK07
0
50
100
Core depth (cm)
50
100
150
close up
Fig. X
b
Core
SK06
Oxcal v4.4.2 Bronk Ramsey (2020); r:5 Atmospheric data from Reimer et al. (2020)
Boundary
Year- 241Am peak_Lauterbach 5.5 cm
R_Date Poz-26363
R_Date Poz-44073
R_Date Poz-26364
R_Date Poz-26366
R_Date Poz-26367
R_Date Poz-26371
R_Date Poz-26375
R_Date Poz-37469
R_Date Poz-26373
R_Date Poz-37471
R_Date Poz-26374
Boundary Bottom
R_Date Poz-26368
R_Date Poz-37470
R_Date Poz-26372
R_Date Poz-26370
241Am activity
TOC bulk
Leaf or plant
rejected date
P_Sequence(1,2)
Depth (cm)
0
50
100
150
200
10000
8000
6000
4000
2000
0
Age cal. yr BP

Figure 2

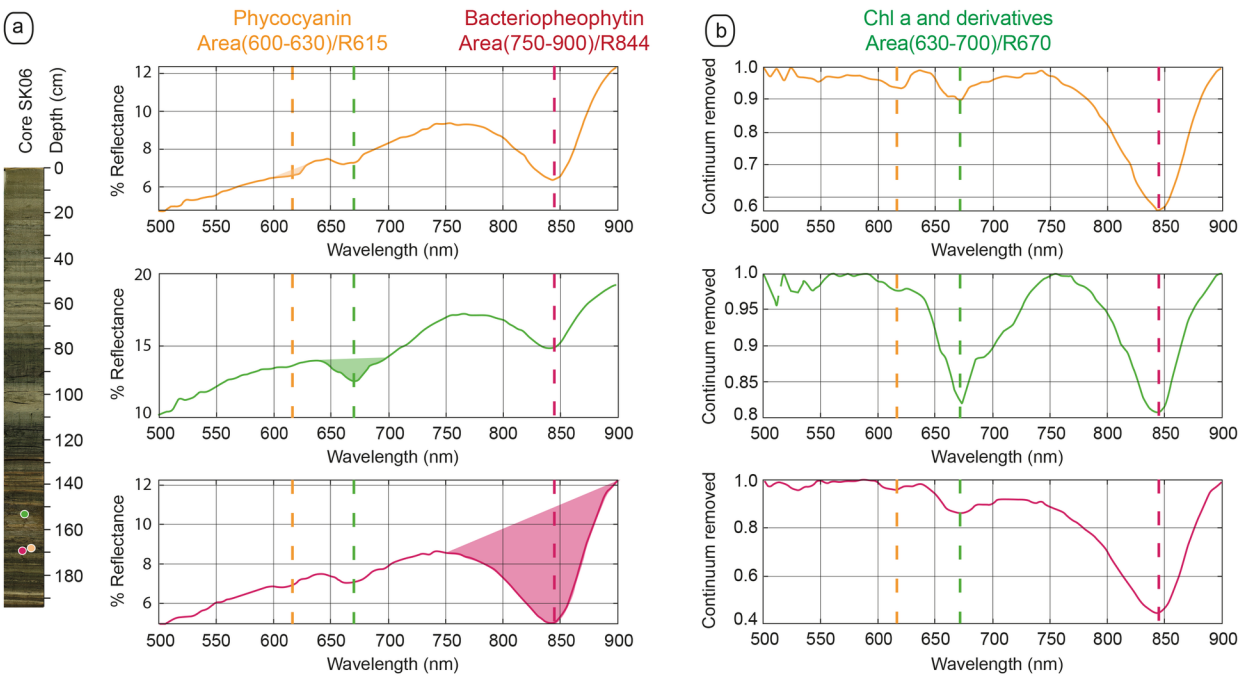
a
Phycocyanin
Area(600-630)/R615
Bacteriopheophytin
Area(750-900)/R844
b
Chl a and derivatives
Area(630-700)/R670
Core SK06
Depth (cm)
% Reflectance
Continuum removed
Wavelength (nm)

Figure 3

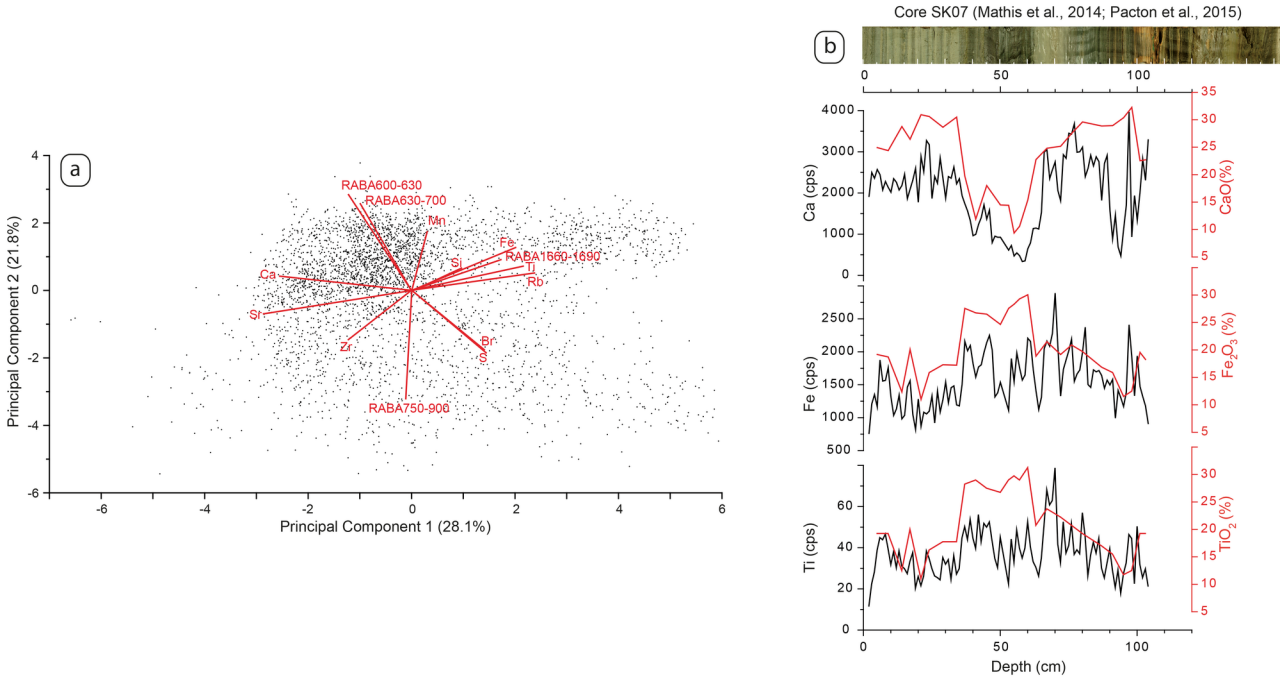
a
RABA600-630
RABA630-700
Mn
Fe
RABA1660-1690
Si
Ti
Rb
Ca
Sr
Zr
Br
K
RABA750-900
Principal Component 2 (21.8%)
Principal Component 1 (28.1%)
b
Core SK07 (Mathis et al., 2014; Pacton et al., 2015)
Ca (cps)
CaO(%)
Fe (cps)
Fe_2O_3 (%)
Ti (cps)
TiO_2 (%)
Depth (cm)

Figure 4

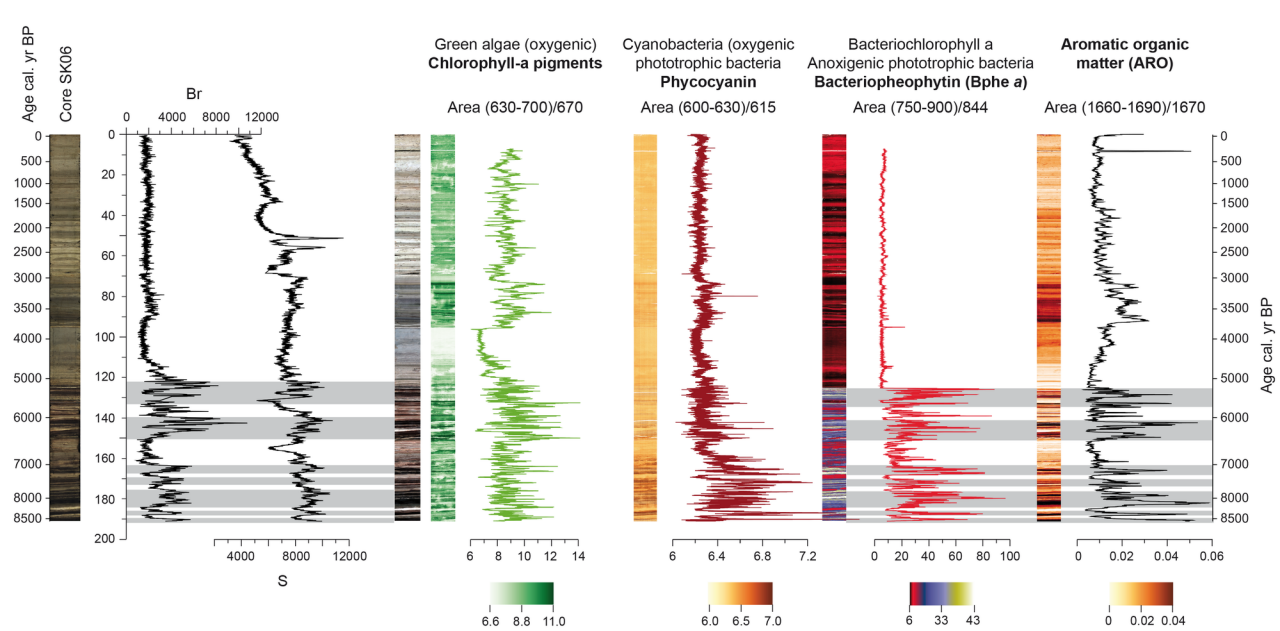
Age cal. yr BP
Core SK06
Br
0 4000 8000 12000
S
4000 8000 12000
Green algae (oxygenic)
Chlorophyll-a pigments
Area (630-700)/670
6 8 10 12 14
6.6 8.8 11.0
Cyanobacteria (oxygenic
phototrophic bacteria
Phycocyanin
Area (600-630)/615
6 6.4 6.8 7.2
6.0 6.5 7.0
Bacteriochlorophyll a
Anoxigenic phototrophic bacteria
Bacteriopheophytin (Bphe a)
Area (750-900)/844
0 20 40 60 80 100
6 33 43
Aromatic organic
matter (ARO)
Area (1660-1690)/1670
0 0.02 0.04 0.06
0 0.02 0.04
0 500 1000 1500 2000 2500 3000 3500 4000 5000 6000 7000 8000 8500
0 20 40 60 80 100 120 140 160 180 200
Age cal. yr BP

Figure 5

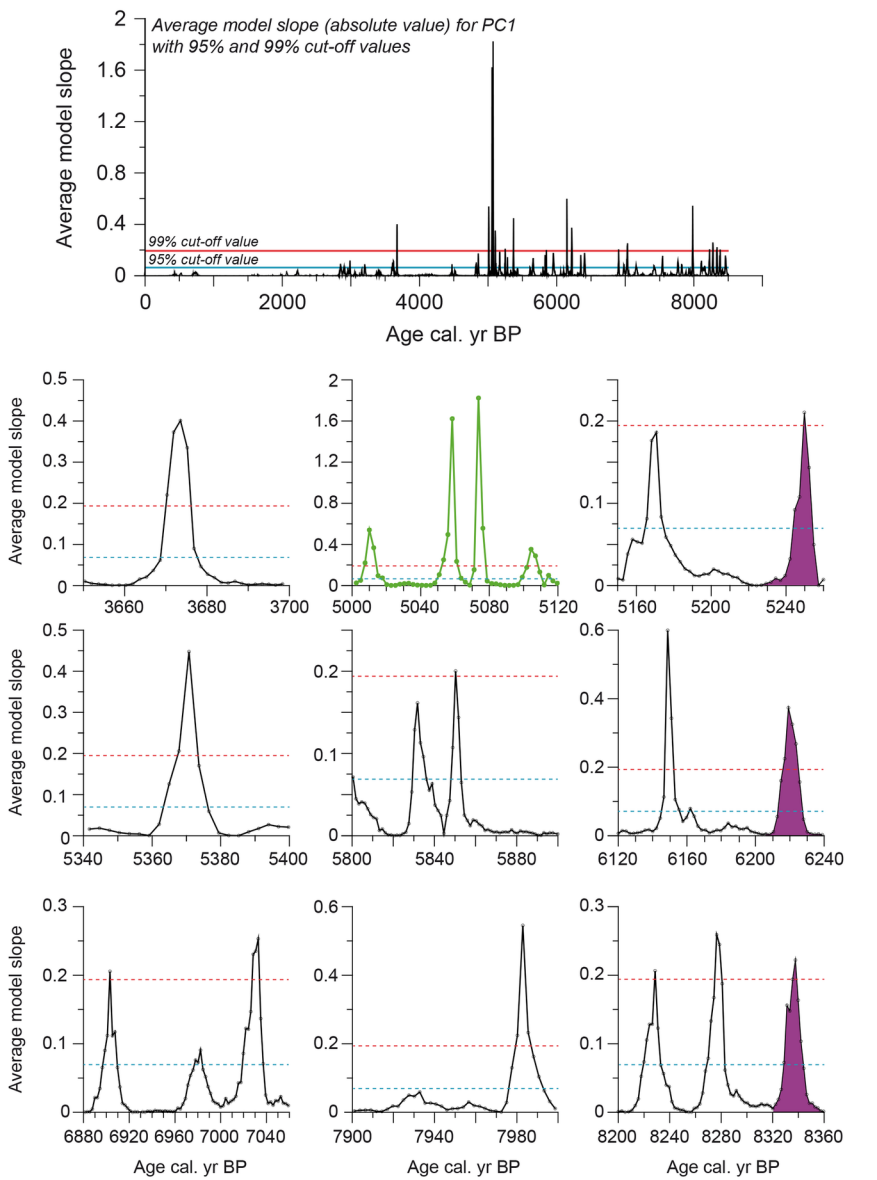
Average model slope (absolute value) for PC1
with 95% and 99% cut-off values
Average model slope
99% cut-off value
95% cut-off value
Age cal. yr BP
Average model slope
Age cal. yr BP

Figure 6

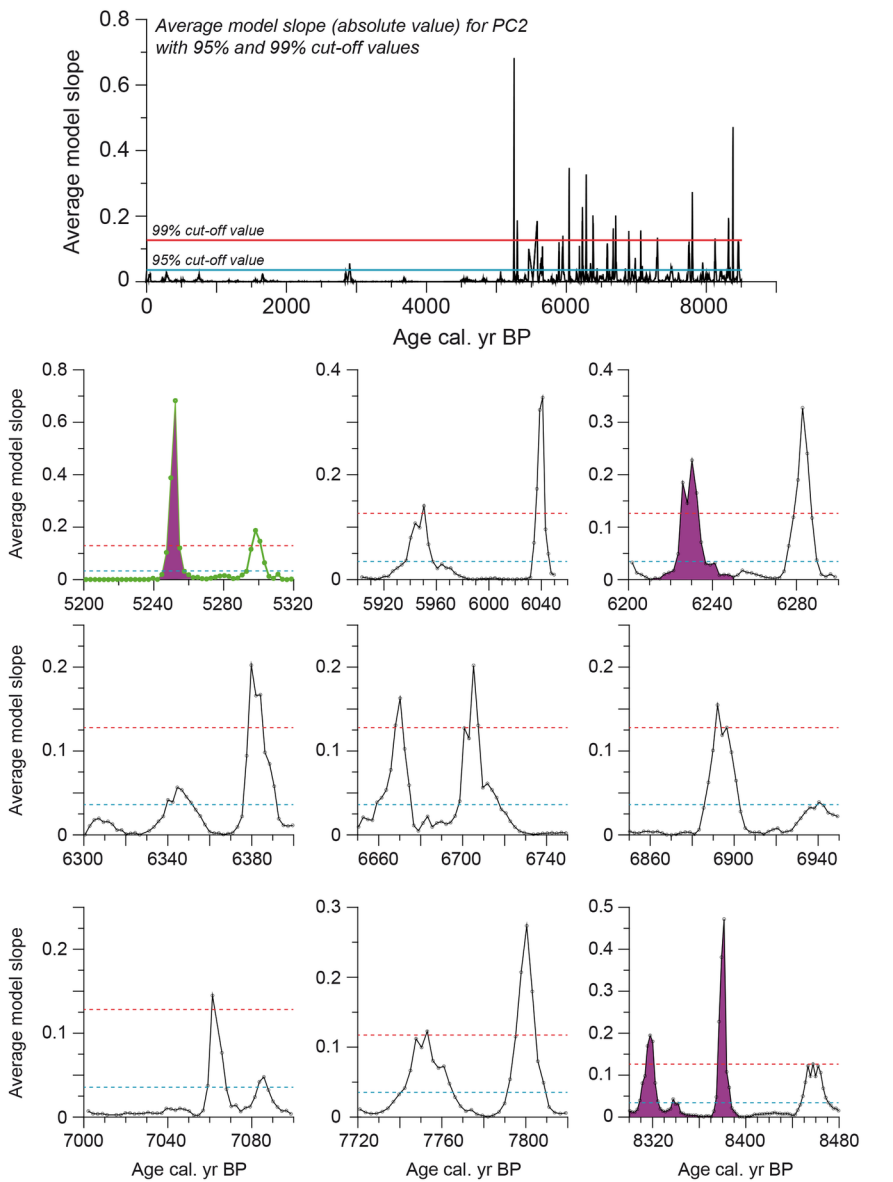
Average model slope (absolute value) for PC2
with 95% and 99% cut-off values
Average model slope
99% cut-off value
95% cut-off value
Age cal. yr BP

Figure 7

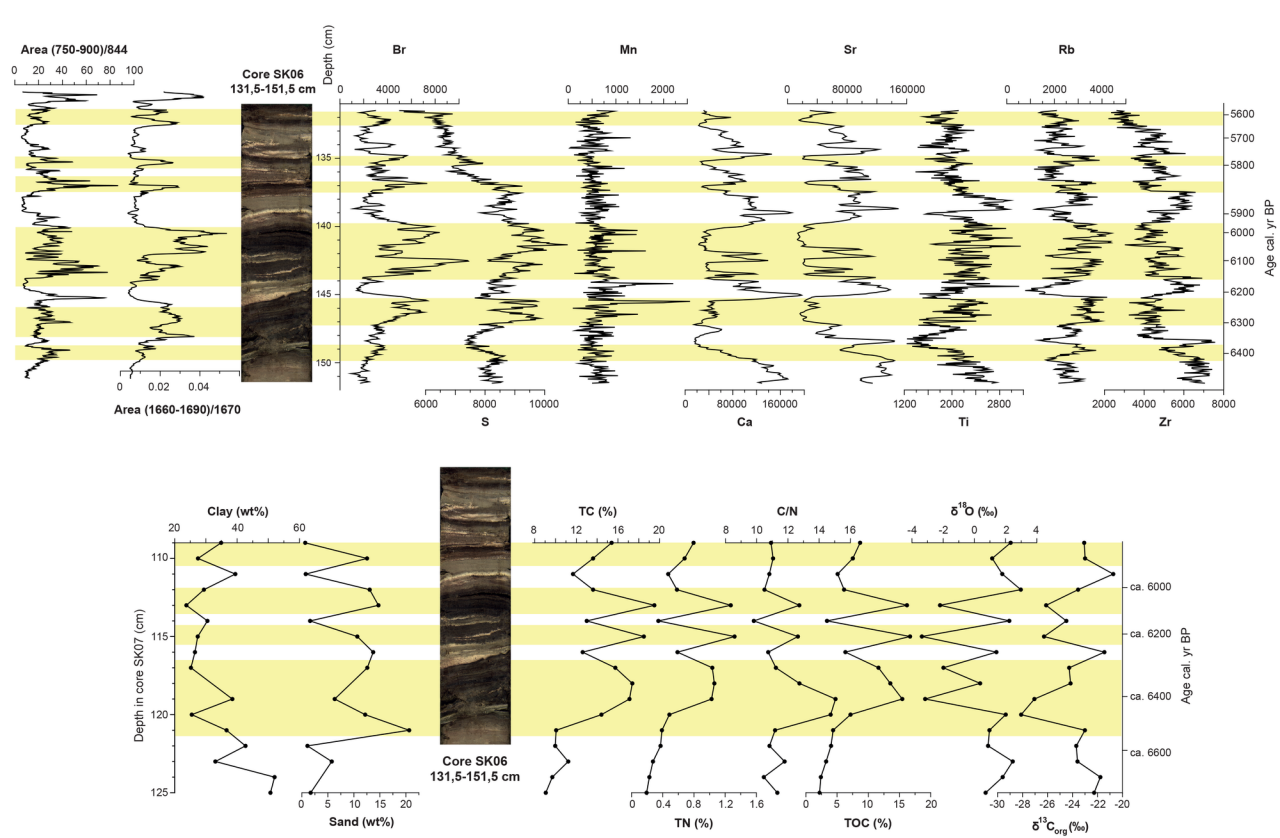
Area (750-900)/844
Core SK06
131,5-151,5 cm
Depth (cm)
Br
Mn
Sr
Rb
Area (1660-1690)/1670
S
Ca
Ti
Zr
Age cal. yr BP
Clay (wt%)
TC (%)
C/N
δ18O (‰)
Depth in core SK07 (cm)
Core SK06
131,5-151,5 cm
Sand (wt%)
TN (%)
TOC (%)
δ13Corg (‰)
ca. 6000
ca. 6200
ca. 6400
ca. 6600
Age cal. yr BP

Figure 8

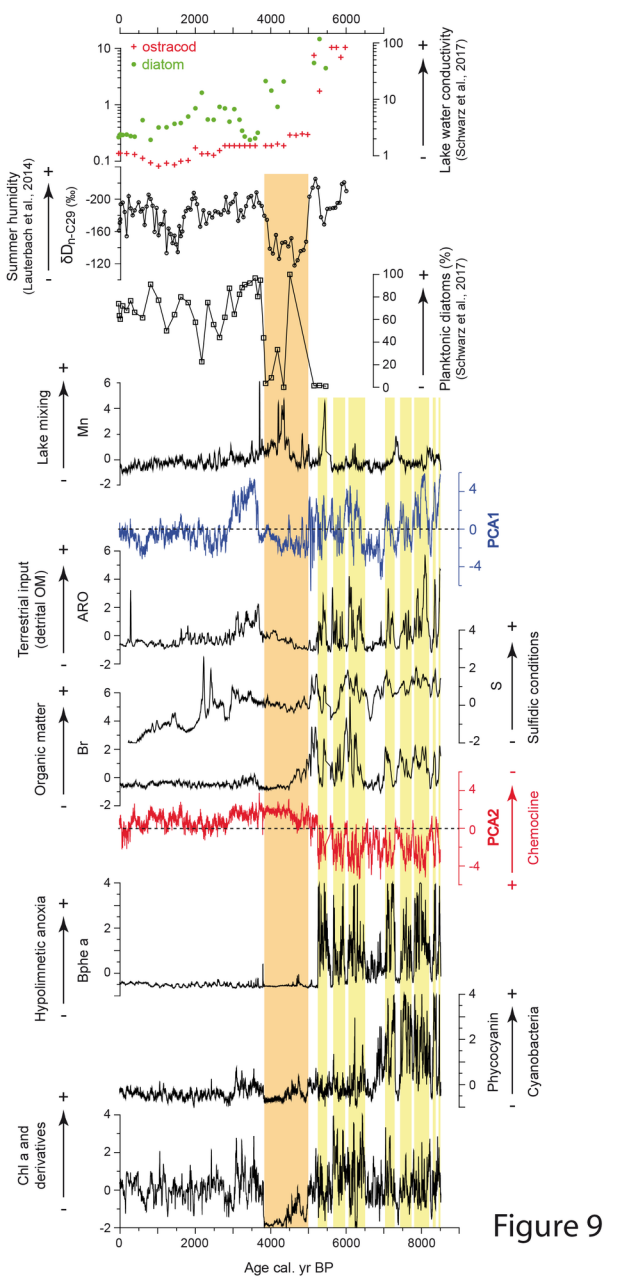
ostracod
diatom
Lake water conductivity (Schwarz et al., 2017)
Summer humidity (Lauterbach et al., 2014)
$\delta D_{n\text{-}C29}$ (‰)
Planktonic diatoms (%) (Schwarz et al., 2017)
Lake mixing
Mn
PCA1
Terrestrial input (detrital OM)
ARO
S
Sulfidic conditions
Organic matter
Br
PCA2
Chemocline
Hypolimnetic anoxia
Bphe a
Phycocyanin
Cyanobacteria
Chl a and derivatives
Age cal. yr BP

Figure 9

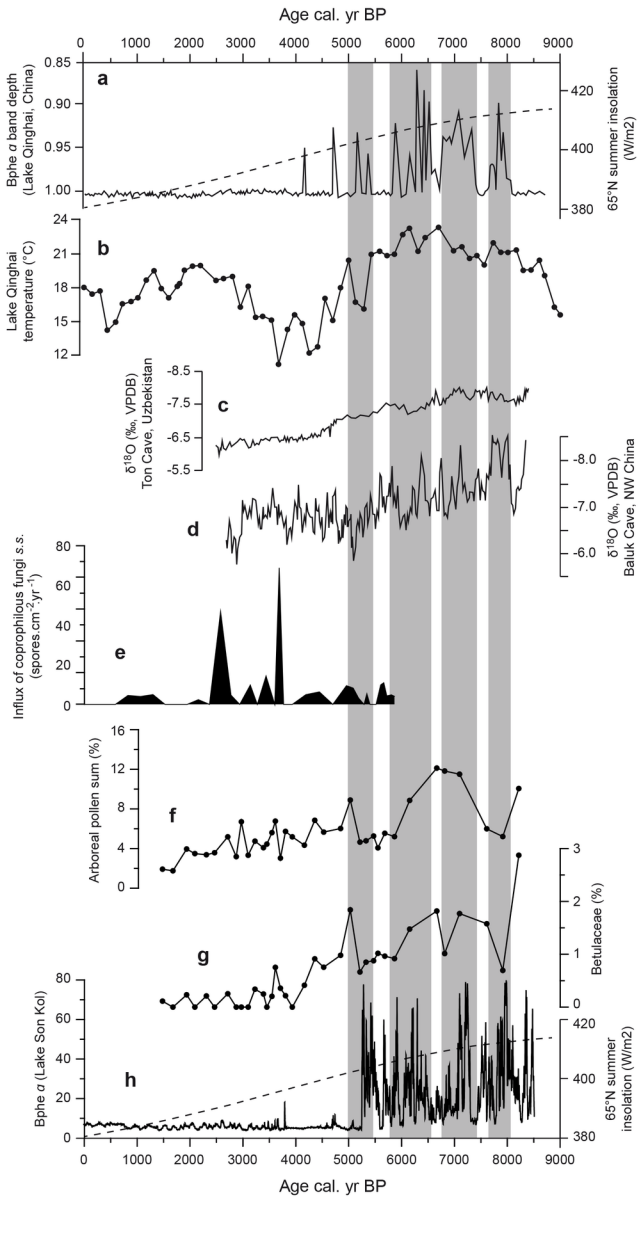
Age cal. yr BP
0
1000
2000
3000
4000
5000
6000
7000
8000
9000
a
Bphe α band depth (Lake Qinghai, China)
0.85
0.90
0.95
1.00
65°N summer insolation (W/m2)
420
400
380
b
Lake Qinghai temperature (°C)
24
21
18
15
12
c
δ18O (‰, VPDB) Ton Cave, Uzbekistan
-8.5
-7.5
-6.5
-5.5
d
δ18O (‰, VPDB) Baluk Cave, NW China
-8.0
-7.0
-6.0
e
Influx of coprophilous fungi s.s. (spores.cm-2.yr-1)
80
60
40
20
0
f
Arboreal pollen sum (%)
16
12
8
4
0
g
Betulaceae (%)
3
2
1
0
h
Bphe α (Lake Son Kol)
80
60
40
20
0
65°N summer insolation (W/m2)
420
400
380
0
1000
2000
3000
4000
5000
6000
7000
8000
9000
Age cal. yr BP

Figure 10

Lab. ID	Sampling interval	Dated material	**Correlation LITHO in Core SK6 (cm)**	AMS ^{14}C age (yr BP + σ)	Corr. AMS ^{14}C age (yr BP + σ)	Calibrated age (cal. yr BP + 2σ)
	SONK_11_D1/2 (Lauterbach et al., 2014)	^{241}Am peak (5,5 cm)	2			-13
Poz-26363	**Sonkul 4A 0-75 0-1cm**	**Bulk sediment**	**30**	**2000 ± 30**	**1850 ± 30**	2139**
*Poz-44073	SONK_11_D1/2 (Lauterbach et al., 2014)	Terrestrial plant remains	33	1575 ± 35		
*Poz-26364	Sonkul 4A 0-75 30-31cm	Bulk sediment	63,5	2770 ± 40	2620 ± 40	
*Poz-26366	Sonkul 4A 75-150 0-1cm	Bulk sediment	100	3750 ± 35	3600 ± 35	
*Poz-26367	Sonkul 4A 75-150 20-21cm	Bulk sediment	127	4730 ± 40	4580 ± 40	
*Poz-26371	Sonkul 7A 120-180 0-1cm	Bulk sediment	135	5270 ± 40	5120 ± 40	
Poz-26368	**Sonkul 4A 75-150 40-41cm**	**Bulk sediment**	**137**	**5240 ± 40**	**5090 ± 40**	5817**
*Poz-26375	Sonkul 7A 120-180 5cm	Bulk sediment	139	5250 ± 40	5100 ± 40	
Poz-37470	**Sonkul 7A 120-180 cm 7.2 cm- 8.6cm**	**Bulk sediment**	**141**	**5410 ± 40**	**5260 ± 40**	6052**
*Poz-37469	Sonkul 7A 120-180 cm 7.2 cm- 8.6cm	Terrestrial plant remains	141	5460 ± 40	5310 ± 40	
Poz-26372	**Sonkul 7A 120-180 15.5-16.5cm**	**Bulk sediment**	**149**	**6200 ± 50**	**6050 ± 50**	6900**
Poz-26370	**Sonkul 4A 75-150 65-66cm**	**Bulk sediment**	**167?**	**6790 ± 40**	**6640 ± 40**	7521**
*Poz-26373	Sonkul 7A 120-180 26.5-27.5cm	Bulk sediment	166	6330 ± 50	6180 ± 50	
*Poz-37471	Sonkul 7A 120-180 cm 37.5-38.5cm	Bulk sediment	172	6880 ± 50	6730 ± 50	
*Poz-26374	Sonkul 7A 120-180 45.5-46.3cm	Bulk sediment	184	7570 ± 50	7420 ± 50	

The asterisks (*) denotes the radiocarbon dates applied to establish the age modelling. Bold samples correspond to excluded dates from age-dep
Double asteriks (**) correspond to median probability ages as calculated online with Oxcal8.2